



1

1 **Secondary aerosol formation in marine Arctic environments: A model measurement**
2 **comparison at Ny-Ålesund**

3 Carlton Xavier¹, Metin Baykara^{1,2}, Robin Wollesen de Jonge³, Barbara Altstädter⁴, Petri
4 Clusius¹, Ville Vakkari^{5,6}, Roseline Thakur¹, Lisa Beck¹, Silvia Becagli⁷, Mirko Severi⁷, Rita
5 Traversi⁷, Birgit Wehner⁸, Mikko Sipilä¹, Markku Kulmala¹, Michael Boy¹, Pontus Roldin³

6 ¹Institute for Atmospheric and Earth Systems Research, University of Helsinki, P.O. Box 64,
7 00014 Helsinki, Finland

8 ²Climate and Marine Sciences Department, Eurasia Institute of Earth Sciences, Istanbul
9 Technical University, Maslak 34469, Istanbul, Turkey

10 ³Division of Nuclear Physics, Department of Physics, Lund University, P. O. Box 118 SE-221
11 00 Lund, Sweden

12 ⁴Institute of Flight Guidance, Technische Universität Braunschweig, 38108 Braunschweig,
13 Germany

14 ⁵Atmospheric Chemistry Research Group, Chemical Resource Beneficiation, North-West
15 University, Potchefstroom, South Africa

16 ⁶Finnish Meteorological Institute, POBox 503, FI-00101 Helsinki, Finland

17 ⁷Department of Chemistry, University of Florence, Sesto Fiorentino, 50019 Florence, Italy

18 ⁸Institute of Tropospheric Research, 04318 Leipzig, Germany

19

20 **Correspondence:** Carlton Xavier (carlton.xavier@helsinki.fi) and Pontus Roldin
21 (pontus.roldin@nuclear.lu.se)

22

23 **Abstract**

24 In this study, we modeled the aerosol particle formation along air mass trajectories arriving at
25 the remote Arctic research stations Gruebadet (67 m a.s.l) and Zeppelin (474 m a.s.l), Ny-
26 Ålesund during May 2018. The aim of this study was to improve our understanding of
27 processes governing secondary aerosol formation in remote Arctic marine environments. We
28 run the Lagrangian chemistry transport model ADCHEM, along air mass trajectories
29 generated with FLEXPART v10.4. The air masses arriving at Ny-Ålesund spend most of their
30 time over the open ice-free ocean. In order to capture the secondary aerosol formation from
31 the DMS emitted by phytoplankton on the ocean surface, we implemented a recently
32 developed comprehensive DMS and halogen multi-phase oxidation chemistry scheme,
33 coupled with the widely used Master Chemical Mechanism (MCM).

34 The modeled median particle number size distributions are in close agreement with the
35 observations in the marine influenced boundary layer at near sea surface Gruebadet site.
36 However, while the model reproduces the accumulation mode particle number concentrations
37 at Zeppelin, it overestimates the Aitken mode particle number concentrations by a factor of



2

38 ~5.5. We attribute this to the deficiency of the model to capture the complex orographic
39 effects on the boundary layer dynamics at Ny-Ålesund. The model also reproduces the
40 average vertical particle number concentration profiles within the boundary layer (0-600 m
41 a.s.l.) above Gruvebadet, as measured with Condensation Particle Counters (CPCs) on board
42 an Unmanned Aircraft Systems (UAS).

43 The model successfully reproduces the observed Hoppel minima, often seen in particle
44 number size distributions at Ny-Ålesund. The model also supports the previous experimental
45 findings that ion mediated $\text{H}_2\text{SO}_4\text{-NH}_3$ nucleation can explain the observed new particle
46 formation in the marine Arctic boundary layer in the vicinity of Ny-Ålesund. Precursors
47 resulting from gas and aqueous phase DMS chemistry contribute to the subsequent growth of
48 the secondary aerosols. The growth of particles is primarily driven via H_2SO_4 condensation
49 and formation of methane sulfonic acid (MSA) through the aqueous-phase ozonolysis of
50 methane sulfinic acid (MSIA) in cloud and deliquescent droplets.

51 **1. Introduction**

52 The Earth's radiation budget is influenced both directly and indirectly by aerosols, which
53 scatter and absorb the incoming short-wave radiation (direct effect) and serve as cloud
54 condensation nuclei (CCN, indirect effect), affecting both short and long-wave radiation
55 (Gantt et al., 2014; Oshima et al., 2020; Park et al., 2017; Scott et al., 2014). The Arctic
56 environments are susceptible to perturbations in the radiation balance, with some estimates
57 suggesting that, compared to the global average, the Arctic is warming at twice the rate, a
58 phenomenon termed as Arctic amplification (AMAP, 2011, 2017; Tunved et al., 2013). The
59 warming of the Arctic polar environment has accelerated sea ice loss, leading to a rapid
60 decline in the extent and duration of snow cover and increase in permafrost thaw (AMAP,
61 2011, 2017; Bengtsson et al., 2013).

62 The Arctic aerosol number concentration shows a pronounced seasonal variation, where the
63 late winter and early spring period is characterized by elevated accumulation mode aerosol
64 concentrations, accompanied by trace gases (mostly anthropogenic with long-range
65 transported trace elements such as sulfates, soot, and Peroxy Acyl Nitrates (PANs)). This
66 annually recurring phenomenon in late winter and spring is termed the Arctic Haze (Barrie,
67 1986; Lupi et al., 2016; Tunved et al., 2013). This contrasts with the summer period, when the
68 atmospheric new particle formation is observed at Arctic sites, most likely due to low
69 background aerosol concentrations, increased photo-chemistry and biological activity
70 (Engvall et al., 2008; Heintzenberg et al., 2017; Tunved et al., 2013).



71 The climate change driven Arctic sea ice loss has a profound impact on natural aerosol
72 production. Arrigo and van Dijken, 2015 found that decreasing and thinning of sea ice
73 increased the rates of phytoplankton net primary production by ~20% between the years 1998
74 and 2009. This can lead to an increase in the emissions of primary biogenic precursors such as
75 dimethyl sulfide (DMS), nitrogen volatiles (e.g. alkyl-amines) (Dall’Osto et al., 2017a;
76 Dall’osto et al., 2017b) and biological iodine species (Cuevas et al., 2018). DMS is emitted
77 into the atmosphere via air-sea gas exchanges (Park et al., 2017; Uhlig et al., 2019), and
78 accounts for ~80% of global natural sulfur emissions (Kettle and Andreae, 2000; Uhlig et al.,
79 2019). Methane sulfonic acid (MSA) and sulphuric acid (H_2SO_4) is formed via DMS gas-
80 phase oxidation by OH and halogen species (Cl, Br) (Hoffmann et al., 2016; Kim et al., 2021;
81 Wollesen de Jonge et al., 2021). MSA and H_2SO_4 , together with ammonia (NH_3) or amines,
82 act as precursors contributing to new particle formation (NPF) and subsequently to CCN
83 production, influencing cloud formation and radiative balance (Berndt et al., 2020; Dall’osto et
84 al., 2017; Hoffmann et al., 2016; Kim et al., 2021). NH_3 plays a major role in particle
85 formation through stabilization of sulfuric acid clusters (Beck et al., 2021; Jokinen et al.,
86 2018; Olenius et al., 2013). Depending on local parameters such as ocean pH, salinity and
87 temperature, global oceans can act either as a source or sink of NH_3 (Paulot et al., 2015).
88 Apart from participating in cluster formation, NH_3 influences the pH of marine aerosols by
89 neutralizing the acid (H_2SO_4 and MSA) in the particles (Paulot et al., 2015). Though a few
90 potential sources of NH_3 are known, for example coastal sea bird colonies, pockets of open
91 water and melting sea ice in summertime Arctic, the magnitude of the emissions remain
92 uncertain (Dall’Osto et al., 2019; Riddick et al., 2012; Wentworth et al., 2016).

93 DMS oxidation chemistry has been under focus, but uncertainties in climate predictions
94 persist since the chemical transport models (CTMs) and global climate models (GCMs)
95 employ fixed MSA and SO_2 yields from gas-phase oxidation of DMS to calculate aerosol
96 formation (Hertel et al., 1994; Hoffmann et al., 2016; Kloster et al., 2006; Wollesen de Jonge
97 et al., 2021). Including a detailed multi-phase (aqueous-phase chemistry coupled with gas-
98 phase chemistry) DMS chemistry in numerical models can overcome these uncertainties
99 (Barnes et al., 2006; Campolongo et al., 1999). Reaction intermediates such as dimethyl
100 sulfoxide (DMSO), dimethyl sulfone (DMSO_2), methane sulfinic acid (MSIA) are water-
101 soluble, and experiments have shown that neglecting aqueous phase chemistry leads to either
102 an under-estimation of modeled MSA (Campolongo et al., 1999), or an over-estimation of
103 gaseous SO_2 compared to measured values (Hoffmann et al., 2016). For example, the
104 temperature dependent ratio of MSA/non-sea-salt SO_4^{2-} (nss-SO_4^{2-}) is often used to estimate



4

105 the contribution of DMS to sulfate budget (Ayers et al., 1999; Barnes et al., 2006).
106 Campolongo et al., 1999 showed that modeling studies which included a multi-phase DMS
107 chemistry can bridge the gap between temperature-dependent observations and modeled
108 MSA/nss-SO₄²⁻. Incorporating reactive halogens species over marine environments is crucial
109 in determining the DMS oxidation pathways to either SO₂ or MSA, the aging of marine
110 aerosols and the radiative properties of marine clouds (Hoffmann et al., 2016). Modeling
111 studies have shown that Cl[•] and BrO[•] radicals in the gas phase act as important DMS sinks
112 (Chen et al., 2018; Wollesen de Jonge et al., 2021), further underlining the role of halogen-
113 DMS chemistry in the marine boundary layer.

114 Recent DMS+OH oxidation experiments performed in the AURA chamber at Aarhus
115 University show that MSA dominates the secondary aerosol mass formation (Rosati et al.,
116 2021). Aerosol dynamics model simulations which intended to replicate the observations
117 during these AURA experiments, using the DMS gas-phase chemistry scheme from the
118 Master Chemical Mechanism, MCMv3.3.1, (Jenkin et al., 1997, 2015; Saunders et al., 2003),
119 substantially underestimates the particle mass and number concentrations and the MSA:SO₄
120 (Rosati et al., 2021, Wollesen de Jonge, 2021). Based on these findings, Wollesen de Jonge et
121 al. (2021) developed a new DMS multi-phase chemistry scheme based on MCM v3.3.1,
122 CAPRAM DMS module 1.0 (DM1.0) (Hoffmann et al., 2016), a subset of the multi-phase
123 halogen chemistry mechanism CAPRAM Halogen Module 2.0 (HM2.0) (Bräuer et al., 2013)
124 and new reactions leading to the formation of hydroperoxymethyl thioformate (HPMTF).
125 With the new DMS multi-phase chemistry mechanism, the aerosol dynamics model could
126 capture the observed particle number concentrations and secondary PM MSA and SO₄²⁻
127 during DMS oxidation experiments performed at both dry and humid conditions at 0 °C and
128 20 °C in AURA.

129 In this work, we have implemented the above mentioned DMS multi-phase chemistry
130 mechanism into ADCHEM (see Methods section) and modeled the aerosol formation along
131 air mass trajectories arriving at Ny-Ålesund. We compared the model results with
132 observations from Zeppelin (78°56' N, 11°53' E, 474 m a.s.l) and Gruevbadet (78°92' N, 11°90'
133 E, 67 m a.s.l). These two sites represent remote marine Arctic conditions. Gruevbadet
134 represents ground-level concentrations as it is well within the boundary layer (BL). Zeppelin
135 on the other hand, is most often above the BL in winter months and sometimes below the BL
136 during spring and summer months (Traversi et al., 2020). This implies that Zeppelin is often
137 influenced by long range transport, and Gruevbadet by local short-range effects (Traversi et
138 al., 2020). This, demonstrates the complexity involved in capturing the atmospheric mixing



139 and secondary aerosol concentrations at Ny-Ålesund. The reason is that Svalbard has an
140 orographically complex terrain comprising of mountains, glaciers, fjords and flat lands that
141 introduce various micro-meteorological phenomena (Rader et al., 2021; Schemann and Ebell,
142 2020).

143

144 **2. Methods**

145 Using the combined multi-phase DMS chemistry mechanism by Wollesen de Jonge et al.,
146 (2021), MCMv3.3.1 and the monoterpene peroxy radical autoxidation mechanism (PRAM,
147 Roldin et al., 2019; Xavier et al., 2019) we simulated aerosol particle formation within the
148 marine boundary layer (MBL) upwind and at Ny-Ålesund between 1st - 25th May 2018, using
149 the Aerosol Dynamics, gas and particle-phase CHEMistry and radiative transfer model
150 ADCHEM (Öström et al., 2017; Roldin et al., 2011, 2019). We ran ADCHEM as a
151 Lagrangian model along the air mass trajectories arriving at Zeppelin every 3 hours during the
152 selected period (in total 200 trajectory simulations). FLEXPART v10.4 was used to calculate
153 the air mass trajectories and potential emission sensitivity fields (Pisso et al., 2019; Stohl et
154 al., 2005). The simulation results for the vertical distribution of newly formed aerosol (size <
155 12 nm) were validated against concurrent measurement data available from the ALADINA
156 (Application of Light-Weight Aircraft for Detecting in situ Aerosol) campaign, wherein a
157 UAS was used to investigate horizontal and vertical distribution of aerosol profiles in the
158 marine boundary layer (ABL) (Lampert et al., 2020). Additionally, modeled particle number
159 size distributions and PM₁₀ chemical compositions were compared to the available measured
160 particle number size distributions and PM₁₀ filter samples at both Gruvebadet and Zeppelin
161 measurement stations.

162 **2.1 Air mass trajectories and potential emission sensitivity fields**

163 We employed the Lagrangian particle dispersion model FLEXible PARTicle
164 (FLEXPARTv10.4) to assess the emission sensitivities or “footprints” of air-masses origin
165 arriving at Zeppelin during the simulation period. FLEXPART is a stochastic model used to
166 compute dispersion of hypothetical particles, based on mean, turbulent and diffusive flows
167 which can be run backwards in time to estimate air mass history at a site (Pisso et al., 2019).
168 European Center for Medium-Range Weather Forecasts (ECMWF) ERA5 reanalysis
169 meteorology with 137 height levels, 1-hour temporal and 0.5° x 0.5° spatial resolution, was
170 used as an input to FLEXPART (*ERA5 hourly data on single levels from 1979 to present*).



6

171 *Copernicus Climate Change Service (C3S) Climate Data Store (CDS). last access 30th April*
172 *2021, 10.24381/cds.adbb2d47, ERA5 hourly data on pressure levels from 1979 to present.*
173 *Copernicus Climate Change Service (C3S) Climate Data Store (CDS). last access 30th April*
174 *2021, 10.24381/cds.bd0915c6).* The air-mass history was simulated 7-day backwards in time
175 and arriving at Zeppelin (474 m a.s.l) every 3 hours (at 00:00, 03:00, 06:00, 09:00, 12:00,
176 15:00, 15:00 and 21:00 UTC) for the entire simulation period (1st - 25th May 2018).

177 FLEXPART calculated normalized emission sensitivity fields were combined with oceanic
178 emissions (DMS, dibromomethane, tribromomethane, iodomethane), NH₃ from sea-bird
179 colonies and anthropogenic emissions (NH₃, SO₂, CO, NO_x) derived from global inventories
180 (see section 2.2). This was done to obtain representative emissions that consider the complete
181 emission source regions along the trajectories, upwind of the measurement station.
182 Additional meteorological parameters such as temperature, pressure, sea surface temperature,
183 specific humidity and cloud liquid water content from ERA5 reanalysis dataset were extracted
184 along the trajectories and provided as inputs to ADCHEM.

185

186 **2.2 Gas and primary particle emissions**

187 Emissions of gas-phase biogenic volatile organic compounds (VOCs) α -pinene, β -pinene Δ 3-
188 carene, limonene, isoprene and β -caryophyllene were modeled with a 1 - dimensional version
189 of MEGAN v2.04 (Model of Emissions of Gases and Aerosols from Nature 2.04) (Guenther
190 et al., 2006). Gas-phase emissions of marine halogens such as tribromomethane (CHBr₃),
191 dibromomethane (CH₂Br₂), iodomethane (CH₃I) were retrieved from CAMS-OCE Global
192 oceanic emissions (CAMS-GLOB-OCE) which are available as daily means with a spatial
193 resolution of 0.5°x0.5° (Granier et al., 2019; Ziska et al., 2013). CAMS-GLOB-OCE also
194 provides gas-phase DMS emissions with the same temporal and spatial resolution (Granier et
195 al., 2019) calculated with the air-sea flux parameterization and emission fluxes described in
196 (Lana et al., 2011; Nightingale et al., 2000). NH₃ emissions from seabird colonies were
197 acquired from a global emission inventory (Riddick et al., 2012). To account for additional
198 NH₃ fluxes from the open ocean, we used an estimated sea surface equilibrium NH_{3(g)}
199 saturation concentration of 0.5 nmol/m³ (12.2 ppt at standard temperature and pressure (STP))
200 which approximately correspond to a surface ocean ammonium concentration of 0.125
201 mmol/m³ (or ~3ppb, calculated based on equation 3 & 4 from Wentworth et al., 2016) at a sea
202 surface temperature of +2 °C. The sea surface temperature for the study period varied between
203 0 °C-14 °C along the trajectories. The estimated surface ocean ammonium concentrations is in



204 close agreement with the concentration estimated by the global ocean biogeochemical model
205 COBALT (Stock et al., 2014) in the North Atlantic ocean, but up to a factor of ~5 higher than
206 the concentrations simulated with other ocean biogeochemical models and/or model setups
207 (Paulot et al., 2015). Therefore, we performed model sensitivity runs with a sea surface
208 equilibrium $\text{NH}_{3(\text{g})}$ concentration of 0.1 and 1 nmol/m^3 . The $\text{NH}_{3(\text{g})}$ equilibrium saturation
209 concentrations represent the ambient surface gas-phase concentration at which the air-sea flux
210 changes direction, with a net downward flux from air to sea if the ambient $\text{NH}_{3(\text{g})}$ exceeds the
211 equilibrium gas concentrations and vice versa (Wentworth et al., 2016). For the anthropogenic
212 trace gas and primary particle emissions, we used the CAMS-GLOB-ANT v2.1 inventory,
213 with a spatial resolution of $0.1^\circ \times 0.1^\circ$ (Granier et al., 2019).

214 In this work, we used the sea surface temperature (SST) and wind speed dependent sea-spray
215 aerosol (SSA) emission parameterization by Sofiev et al. (2011), (further referred to as
216 Sofiev11). Sofiev11 used a modified source function based on the parameterization of
217 Monahan et al. (1986) and experiments by Mårtensson et al. (2003) and SEAS campaign by
218 Clarke et al. (2006). The modified source function in Sofiev11 provides extrapolated SSA
219 emissions between size ranges of 10 nm-10 μm , with appropriate correction functions
220 employed for SST deviating from 298.15 K (Sofiev et al., 2011). Sofiev11 SSA
221 parameterization shows that with increasing temperatures, emission flux for larger particles
222 increases while the emission fluxes for smaller particles decreases (Barthel et al., 2019;
223 Sofiev et al., 2011). We performed sensitivity tests using the temperature and wind speed
224 dependent SSA parameterization by Salter et al., (2015), (further referred to as Salter15).
225 Both the Salter15 and Sofiev11 are valid between 10 nm-10 μm . Model simulation
226 comparisons between Sofiev11 and Salter15 have shown that the SSA parameterization from
227 Sofiev11 has a stronger temperature dependence and higher particle number concentration
228 emissions in the Aitken mode but result in lower PM_{10} emissions at temperatures below 25 $^\circ\text{C}$
229 (Barthel et al., 2019).

230

231 **2.2 ADCHEM**

232 For this study, ADCHEM was employed as a 1 - dimensional column model with 40
233 logarithmically vertical layers, extending up to ~2600m. The model time step used for
234 simulations was 30 seconds. The vertical atmospheric turbulent diffusion was solved using a
235 modified Grisogono turbulent diffusivity scheme (Jeričević et al., 2010; Öström et al., 2017;
236 Roldin et al., 2019). The ADCHEM aerosol module includes new particle formation,



237 Brownian coagulation, condensation and evaporation of particles, and finally the dry and wet
238 deposition of both particles and gases. The particle number size distributions were represented
239 using 100 size bins ranging from 1.07 nm to 10 μm dry diameter. Clouds were assumed to be
240 present in the model grid cells when the bulk liquid water content (LWC, extracted along the
241 trajectory from ERA5 datasets) was greater than 0.01 g m^{-3} . As a default, we used a constant
242 cloud supersaturation (S) of 0.5% and the particles were activated into cloud droplets, if the
243 calculated water vapor supersaturation above the particle surface (S_c , calculated using Köhler
244 theory) was smaller than S . During the cloud processing, each activated cloud droplet was
245 assumed to take up an equal amount of liquid water corresponding to the total bulk LWC
246 divided by the calculated number concentration of activated cloud droplets. The gas-liquid
247 droplet mass transfer and dissolution of 50 species in total, including HCl, HNO₃, H₂SO₄,
248 NH₃, HIO₃, H₂O₂, O₃, OH, BrO, NO₃, DMSO, MSIA, MSA and HPMTF and their irreversible
249 reactions in the interstitial and activated cloud droplets are treated by the multi-phase
250 chemistry mechanism (see Wollesen de Jonge et al. (2021) for details). The kinetic pre-
251 processor (KPP) (Damian et al., 2002) was used to generate the multi-phase chemistry
252 mechanism used in this study.

253 Recent observations of NPF at Ny-Ålesund have confirmed the importance of ion-mediated
254 H₂SO₄-NH₃ nucleation in spring with MSA and H₂SO₄ condensation contributing to the
255 subsequent growth of particles (Beck et al., 2021; Lee et al., 2020). In this work, the
256 Atmosphere Cluster Dynamics Code (ACDC) (McGrath et al., 2012; Olenius et al., 2013) was
257 coupled with ADCHEM (Roldin et al., 2019). ACDC was used to model NPF, which
258 involved H₂SO₄ clustering with NH₃ via both neutral and ion-induced pathways with an
259 ionization rate of 1.7 $\text{cm}^{-3}\text{s}^{-1}$. ACDC was used to solve the evolution of molecular H₂SO₄-NH₃
260 clusters by considering the loss of clusters by collisions, evaporation or coagulation
261 scavenging onto larger aerosol particles. At each time step, the flux of clusters (up to ~ 5
262 H₂SO₄ and 5 NH₃ each) growing out of the ACDC molecule-cluster domain represents the
263 NPF rate. These newly formed clusters are assigned to the corresponding smallest particle
264 size bin at 1.07 nm in diameter in ADCHEM, which then simulates the condensational growth
265 of particles and losses due to evaporation, coagulation, and wet and dry deposition.

266 For all simulations, we used model output from the closest height levels which can represent
267 Grubebadet (model height of 73.5 m a.s.l) and Zeppelin (model height of 486.0 m a.s.l).

268 Sensitivity Tests

269 Alongside the main ADCHEM simulations, *BaseCase*, we performed nine complementary



270 scenario runs to assess the impact of different processes on the modeled aerosol
271 concentrations. We performed simulations without aerosol in-cloud processing (*Cloudoff*), to
272 check the impact of in-cloud processing on the growth of aerosols. We investigated the effect
273 of higher PM_{10} particle emissions on the chemical composition of secondary aerosols, using
274 the sea-spray emission parameterization based on Salter et al., 2015 (*SalterSSA*). Simulations
275 were conducted to assess the impact of lower and higher ammonia sources over the open
276 ocean (*LowNH₃*, *HighNH₃*). A sensitivity test without precipitation (*NoPrecip*) was performed
277 to test the influence of precipitation on number concentration and particle composition. Since
278 cloud supersaturation is critical to the activation of particles and is highly uncertain, we
279 performed two simulations with low and high cloud supersaturation ($S=0.2\%$, $SSat=0.2$ and
280 $S=0.8\%$, $SSat=0.8$) to test its impact on the modelled particle distributions. We performed a
281 simulation without new particle formation (*NPFoff*), and finally one simulation without the
282 dissolution and irreversible aqueous chemistry of the intermediate DMS oxidation products,
283 SO_2 and halogens (*woDissolution*), implying that MSA, H_2SO_4 and HIO_3 is only formed in the
284 gas-phase. Table 1. summarizes the setup for different model sensitivity test.

285

286 **Table 1.** Model sensitivity tests performed alongside the main *BaseCase* simulations to test
287 the effect of different parameters on secondary aerosol formation. These sensitivity tests focus
288 on the role of in-cloud processing and aqueous phase chemistry, the NH_3 emissions from open
289 ocean, SSA parameterization and cloud supersaturation. The sea surface equilibrium $NH_{3(g)}$
290 concentrations in ppt are provided in the brackets.

Simulation	In-cloud Processing	$NH_{3(\text{equilibrium})}$ ($nmol/m^3$, ppt)	SSA parameterization	Precipitation
<i>BaseCase</i>	On	0.5 (12.2)	Sofiev11	On
<i>SalterSSA</i>	On	0.5 (12.2)	Salter 15	On



<i>Cloudoff</i>	Off	0.5 (12.2)	Sofiev11	On
<i>LowNH₃</i> <i>HighNH₃</i>	On	0.1 (2.4) 1 (24)	Sofiev11	On
<i>NoPrecip</i>	On	0.5 (12.2)	Sofiev11	Off
<i>SSat0.8, SSat0.2</i>	On	0.5 (12.2)	Sofiev11	On
<i>NPFoff</i>	On	0.5 (12.2)	Sofiev11	On
<i>WoDissolution</i>	On, but no dissolution and irreversible chemistry of intermediate DMS oxidation products	0.5 (12.2)	Sofiev11	On

291

292 2.3 Measurements

293 We utilized comprehensive measurements from the Ny-Ålesund sites, Zeppelin and
294 Gruvebadet during the period of 1st - 25th May 2018. Since 2017, the atmospheric observatory
295 at Gruvebadet, which is located about 700 m southwest of Ny-Ålesund village at almost sea
296 level (67 m.s.l), hosted Neutral cluster and Air Ion Spectrometer (NAIS, Manninen et al.,
297 2010; Mirme and Mirme, 2013) for semi-permanent measurements. Here we use NAIS
298 measured number size distribution of naturally charged (ions) in diameter size ranges between
299 0.8 nm-40 nm and neutral particles in the size range of 2.5 nm-42 nm, with a temporal
300 resolution of two seconds.



301 During the measurement period, a scanning mobility particle sizer (SMPS), was operated to
302 measure particle number size distribution in the diameter size range of 10 - 470 nm at
303 Zeppelin. Concurrent SMPS data (TSI 3034, 54 channels) with diameter size ranging from 10
304 to 470 nm from Gruvebadet were also available (Dall'osto et al., 2019; Moroni et al., 2020),
305 thus, enabling us to compare the modeled particle number size distribution with the measured
306 size distributions at both measurement stations. Daily resolution continuous aerosol samples
307 with PM₁₀ cutoff were collected at Gruvebadet using a Tecore Skypost low-volume sampler
308 (Amore et al., 2022). The detection limit for Na⁺ was 0.0001 µg m⁻³ and 0.0002 µg m⁻³ for Cl⁻,
309 NH₄⁺ and SO₄²⁻. Since the field blank medians at Gruvebadet were less than 1 percentile of
310 sampled values, the field blanks were not subtracted from the sampled values (Amore et al.,
311 2022).

312 Vertical particle number concentration profiles were obtained using UAS ALADINA (Bärfuss
313 et al., 2018; Lampert et al., 2020), which was operated during the simulation period.
314 ALADINA were operated up to a height of 850 m a.s.l., thus can be used for a potential
315 closure between the two different research sites of Gruvebadet and Zeppelin. ALADINA is
316 equipped with two condensation particle counters (CPCs Model 3007, TSI Inc., St. Paul,
317 MN, USA), measuring in the size ranges of 3 nm - 2 µm (CPC1) and ~12 nm - 2 µm (CPC2)
318 (Lampert et al., 2020; Petäjä et al., 2020). The difference between CPC1 and CPC2 provides
319 an estimate of particle number concentrations in the size of 3 - 12 nm (PN₃₋₁₂), which was
320 used as an indicator of NPF. Alongside the CPCs, a host of other instruments measuring
321 meteorological parameters were operated in unison, the description of which can be found in
322 Bärfuss et al., (2018) and Lampert et al.,(2020).

323 **Evaluating temporal aspects of model performance**

324 The modeled PM₁₀ inorganic chemical composition was evaluated against the measured PM₁₀
325 inorganic chemical composition using statistical estimates such as, normalized mean bias
326 (NMB), Pearson correlation coefficient (r), root mean squared error (RMSE) and fraction of
327 predictions within a factor of 2 of the observed values (FAC2). These tests were used to
328 evaluate modeled values (M_i) against observation values (O_i) at both the measurement sites.

329 Pearson correlation coefficient was calculated using the formula:

$$330 \quad r = \frac{1}{n} \sum_{i=1}^n \frac{(O_i - \bar{O})}{\sigma_O} \frac{(M_i - \bar{M})}{\sigma_M} \quad (\text{Eq 1})$$

331

332 Where σ_o and σ_M are standard deviations of the observed and modeled values, respectively.



12

333 Normalized mean bias (NMB) indicates if the predictions are over or underestimating the
334 observed values, with the factor representing the under or over estimation. NMB was
335 calculated using Eq. 2:

$$NMB = \frac{\sum_{i=1}^n (M_i - O_i)}{\sum_{i=1}^n O_i} \quad (\text{Eq 2})$$

336
337

338 Root mean squared error (RMSE) was calculated using Eq. 3:

$$RMSE = \sqrt{\frac{\sum_{i=1}^n (M_i - O_i)^2}{n}} \quad (\text{Eq 3})$$

340

341 FAC2 is a robust metric defined as the percentage of predictions which are within a factor of
342 2 of the observed values (Eq. 4):

$$Fac2 = 0.5 \leq \frac{M}{O} \leq 2.0 \quad (\text{Eq 4})$$

343

344 3. Results and Discussion

345 In the following sections, we analyze and evaluate the model results against comprehensive
346 measurements in Ny-Ålesund. In sub-section 3.1, we focus on the particle number size
347 distributions at both sites, followed by gas-phase concentrations and PM₁₀ inorganic chemical
348 composition (sub-section 3.2) and the vertical nano-particle concentration profiles (sub-
349 section 3.3). Finally, in sub-section 3.4, we analyze the results from the model sensitivity
350 tests.

351

352 3.1 Particle number size distributions

353 Figure 1(a) and (b) show the observed and predicted particle number size distributions at
354 Gruvebadet for the *BaseCase* simulation. Figure 1(a) includes SMPS observations starting
355 from 10 to 470 nm and NAIS observations for neutral particles in the range 2.5 nm-10 nm
356 (boundary marked by the black line) since NAIS data below 2.5 nm cannot be relied upon,
357 owing to the presence of corona generated ions (Jayaratne et al., 2017; Manninen et al., 2011,
358 2016).

359 In the *BaseCase* simulations, ADCHEM reproduces the general trends of the observed
360 particle number concentrations. For example, the model captures particle formation on 2nd



361 May followed by an increasing number of Aitken and accumulation mode particles during the
362 days of 3rd - 4th May, which is the result of more polluted air masses arriving at Ny-Ålesund
363 from the European continent (Figure S1). Similarly, the model reproduces the particle
364 formation on the 20th of May, specifically in the size ranges 2-8 nm, but overestimates the
365 Aitken mode and accumulation mode particle concentration on the 21st of May. In general, the
366 model predicts the formation of new particles with reasonable accuracy during the selected
367 period. However, the model tends to underestimate the nucleation mode particle number
368 concentrations between 10-25 nm ($PN_{10-25\text{ nm}}$) around noon, and overestimate the
369 concentrations during the morning and evening (Figure 2a). The model and measurements
370 show an apparent time delay in the formation of new particles larger than 10 nm. While the
371 measurements show a peak at 11 am the simulated $PN_{10-25\text{ nm}}$ shows a maximum at 3 am and 6
372 pm. The modeled $PN_{10-25\text{ nm}}$ maximum around 6 pm is likely a result of the formation of new
373 particles around noon, which grow to >10 nm in diameter during the afternoon and evening
374 by condensation of H_2SO_4 . The predicted Aitken ($PN_{25-100\text{ nm}}$) and accumulation mode particle
375 concentrations ($PN_{>100\text{ nm}}$) which form few days upwind of the station are overall, in good
376 agreement with the measurements, which show a minor diurnal trend (Figure 2b-c). The
377 measurements indicate that at Gruvebadet, $PN_{10-25\text{ nm}}$ contributes the most significant fraction
378 of measured total number concentrations with 45.3%, while $PN_{25-100\text{ nm}}$ and $PN_{100-470\text{ nm}}$
379 contribute 30.5% and 23.94% respectively. However, the simulations predict greater
380 contribution of Aitken mode (~53.85%) to total number concentration, with the $PN_{10-25\text{ nm}}$ and
381 $PN_{100-470\text{ nm}}$ accounting for ~ 36.58% and 9.57% respectively (Figure S2).

382 Figure 2 shows the measured size distribution in panel (a) and simulated size distribution in
383 panel (b) for Zeppelin. At Zeppelin, the model overestimates the number concentration in
384 nucleation and Aitken modes (also cf. Figure S3, supplementary). The particle number size
385 distribution measurements at Zeppelin indicate that the relative contribution of the three
386 modes (nucleation, Aitken and accumulation) varies to some extent when compared to
387 Gruvebadet. Measurements show that at Zeppelin, $PN_{10-25\text{ nm}}$ contributes ~33.46%, $PN_{25-100\text{ nm}}$
388 46.43% and $PN_{>100\text{ nm}}$ 20.11% to the total particle number concentrations. The model predicts
389 lower relative contribution of $PN_{10-25\text{ nm}}$ (26.94%), and a greater contribution of $PN_{25-100\text{ nm}}$
390 (63.44%) to the total simulated particle number concentrations. The diurnal trends at Zeppelin
391 agree well with earlier measurements conducted at Zeppelin in spring by Ström et al. (2009).
392 Additionally, the measured diurnal pattern at Zeppelin varies in comparison to Gruvebadet. At
393 Zeppelin, the $PN_{10-25\text{ nm}}$ concentrations peak in the afternoon and evening. The modeled
394 $PN_{10-25\text{ nm}}$ shows only a weak diurnal trend. It should be noted that the measurements show a

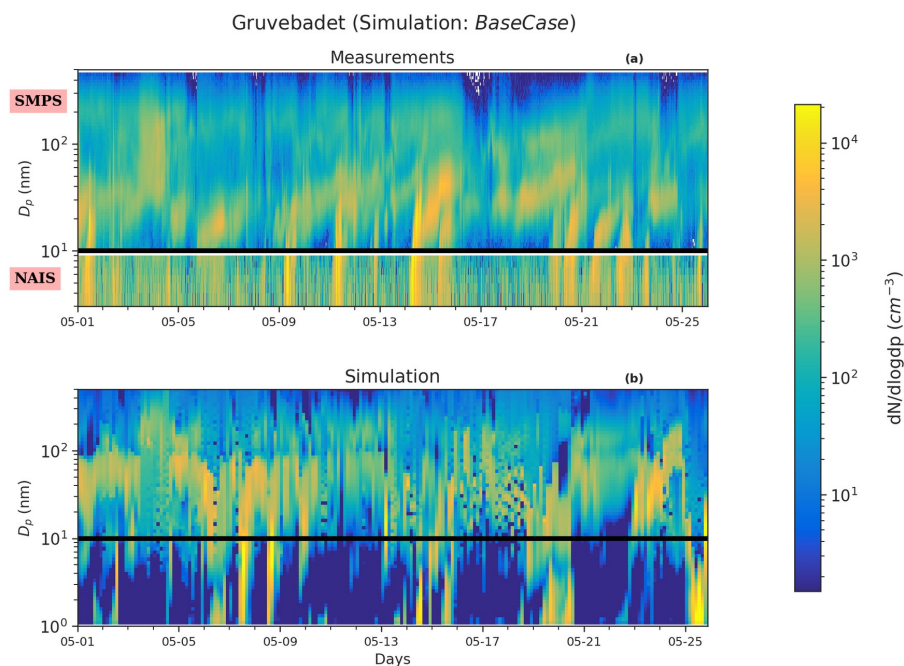


395 time delay of around 3 hours in the peak $PN_{10-25\text{ nm}}$ concentrations at the two sites (Figure S2
396 and S3). This is possibly be a result of vertical mixing and dilution effects modulating the
397 observed particle number concentrations at sites situated at different altitudes, similar to
398 observation made at Zeppelin and Corbel by Ström et al. (2009).

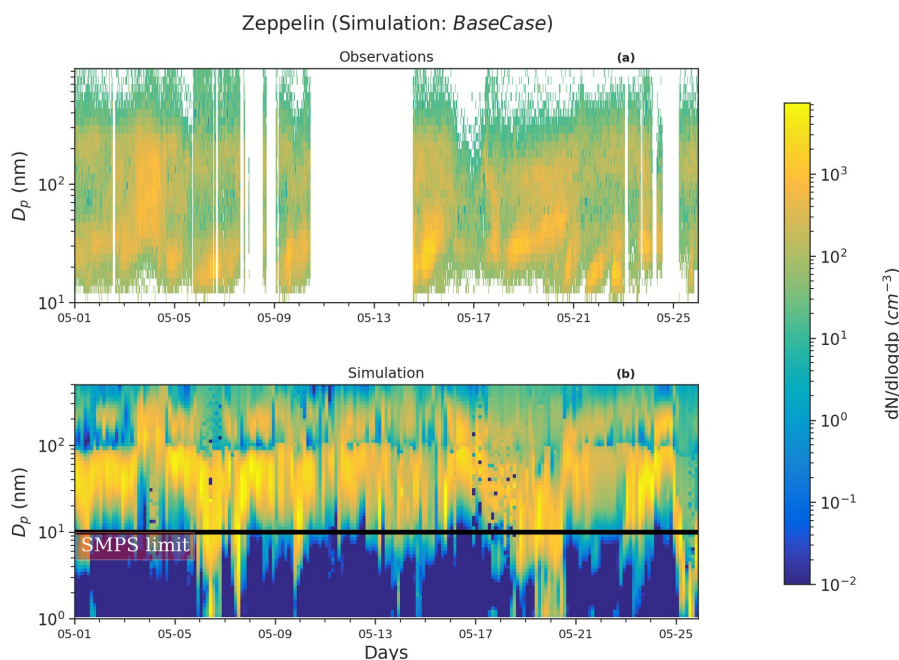
399 ADCHEM considers the formation of new particles via both the ion-mediated and neutral
400 $H_2SO_4-NH_3$ clustering pathways. Beck et al (2021) observed dominant contribution of
401 negative $H_2SO_4-NH_3$ clusters to secondary particle formation in May 2017 at Ny-Ålesund,
402 with HIO_3 playing a small role in the initial particle formation. However, the discrepancy in
403 the modeled and observed diurnal trends of $PN_{10-25\text{ nm}}$ could indicate that there are other
404 sources or vapors that might potentially contribute to the particle formation. Other possible
405 NPF mechanism may involve amines (Olenius et al., 2013) and pure biogenic highly oxidized
406 molecule (HOM) (neutral and ion induced) nucleation (Kirkby et al., 2016). We speculate that
407 the exclusion of these other mechanisms (HIO_3 , H_2SO_4 -amines and HOM driven particle
408 formation) might result in the discrepancies in the modeled and observed particle number
409 concentration diurnal trends. HIO_3 induced particle formation could, e.g. play an important
410 role if the air masses upwind of Ny-Ålesund traverse over the sea-ice covered regions
411 (Baccarini et al., 2020; Beck et al., 2021).



15



412 **Figure 1.** Particle number size distribution at Gruvebadet for *BaseCase*. The panel (a) shows
413 the measurement data for the period 1-25th May from SMPS (10 nm-470 nm) and NAIS (2.5 -
414 10 nm) and the panel (b) provides the modeled particle size distribution. The black line at 10
415 nm denotes the boundary above which SMPS data starts and NAIS data ends. The abscissa
416 indicates the time for the entire simulated duration. The ordinate in Figure 1 for both panels
417 (a) and (b) indicates the particle diameter (D_p , nm).



419 **Figure 2.** Particle size distribution at Zeppelin. The panel (a) shows the measurement data for
420 the period 1-25th May from SMPS and the panel (b) provides the simulated particle size
421 distribution for the *BaseCase* simulations. The abscissa and ordinates are similar to Figure 1.

422

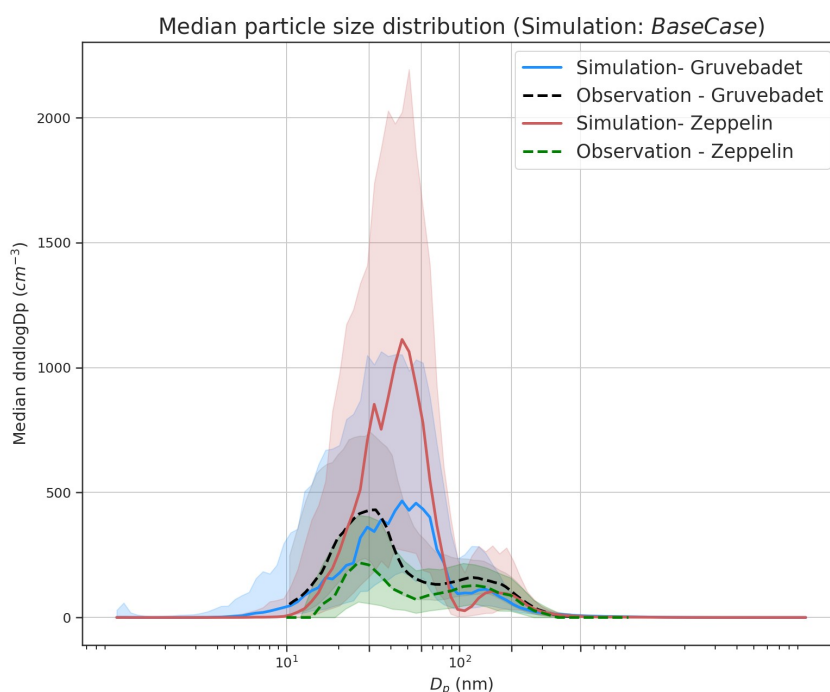
423 Figure 3 presents the median particle number size distribution for the *BaseCase* simulation at
424 both Zeppelin and Gruebadet, with respective 25th and 75th percentiles, for the entire selected
425 period. At Gruebadet, the modeled and measured median particle number size distributions
426 are in reasonable agreement for both Aitken and accumulation mode. However, the model
427 over predicts the median Aitken mode concentrations at Zeppelin by a factor ~ 5.5 . The
428 modeled Aitken mode peak at both measurement sites is ~ 50 nm, while the measured Aitken
429 mode peak is ~ 30 nm. Though the modeled accumulation mode peak is at a larger size (~ 150
430 nm), compared to the measured accumulation mode peak (~ 110 nm), the predicted values are
431 in good agreement with the monthly averaged accumulation mode peak location measured at
432 Zeppelin in earlier studies (~ 160 - 170 nm, Dall'Osto et al., 2019).

433 The discrepancy between the modeled and measured particle concentrations at Zeppelin can



17

434 be caused by the underlying complexity of modeling the boundary layer dynamics at an
435 elevated site, such as Zeppelin. The vertical mixing of aerosols along the up-slope or down-
436 slope of a mountain site is difficult, if not impossible for a 1- dimensional column model,
437 since it is unable to capture the topographical influence on locally varying wind speeds or
438 latent and sensible heat fluxes (Mikkola, 2020; Wainwright et al., 2012).



439 **Figure 3.** Median particle number size distribution at Gruvebadet and Zeppelin for both
440 modeled (*BaseCase* simulations) and measured values. The shaded areas indicate the 25th and
441 75th percentiles for both model and measured median particle number size distribution. At
442 Zeppelin, the simulated median size distribution is calculated for periods only when SMPS
443 data were available.

444

445 Another detectable feature in the median particle number size distribution is the diameter of
446 the Hoppel minimum (Hoppel et al., 1985, 1986), and the role of in-cloud processing in
447 forming this minimum. A Hoppel minimum is often observed in marine air masses (Fossum
448 et al., 2018; Tunved et al., 2013; Zheng et al., 2018) and is attributed to in-cloud processing of



449 aerosols, with chemical processing (e.g., sulfate production via oxidation of dissolved SO₂)
450 (Feingold and Kreidenweis, 2000; Hoppel et al., 1986), and coalescence of droplets playing a
451 key role (Flossmann and Wobrock, 2019; Hoppel et al., 1986; Hoppel and Frick, 1990; Noble
452 and Hudson, 2013). It has been estimated that, on average, aerosols take part in about 10 non-
453 precipitating cloud cycles before it is removed from the atmosphere by wet scavenging
454 (Hoose et al., 2008; Hoppel et al., 1986; Rosenfeld et al., 2014). These non-precipitating
455 cloud cycles facilitate the formation of hygroscopic accumulation mode particles, with low
456 critical supersaturation (S_c) that readily activates to cloud droplets during subsequent cloud
457 cycles, thus growing to larger sizes. This is because the activated particles undergo chemical
458 processing, gas-to-particle conversions, coalescence and coagulation with other interstitial
459 particles. Upon evaporation of water, the emerging dry particles have a larger size and lower
460 S_c , leading to a minimum being formed between the un-activated and activated cloud droplets
461 (Herenz et al., 2018; Hudson et al., 2015; Noble and Hudson, 2013). The diameter at which
462 the Hoppel minimum is observed varies depending on the cloud supersaturation and particle
463 composition (Hoppel et al., 1986; Hudson et al., 2015), with Hoppel minima sizes observed in
464 ranges from 60 nm at Zeppelin Ny-Ålesund to around 90 nm at Tuktoyatuk, Canada (Herenz
465 et al., 2018; Tunved et al., 2013).

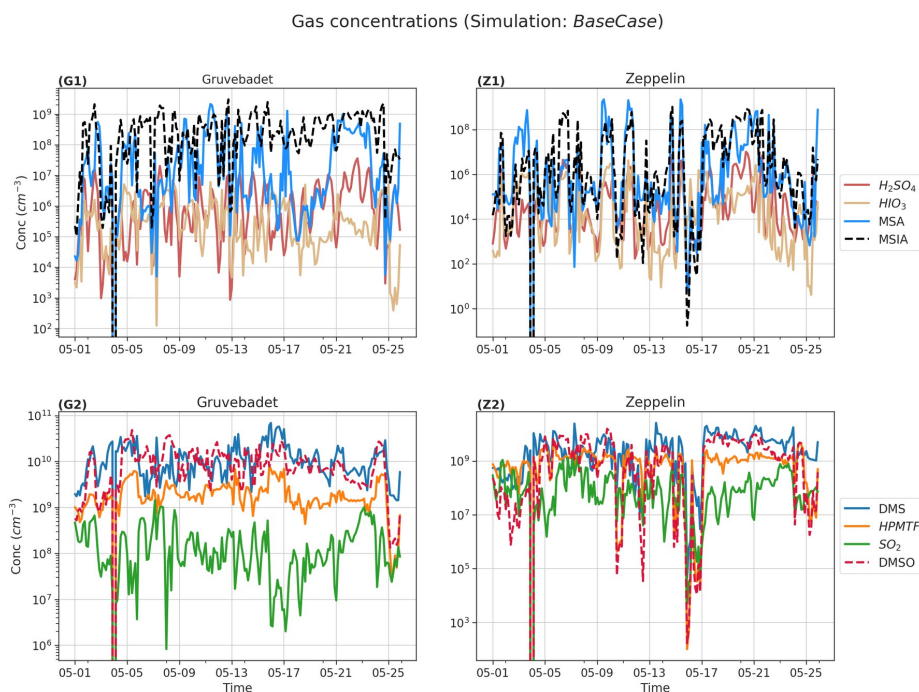
466 The median particle number size distribution in Figure 3 shows that at both stations, the
467 measured Hoppel minima is around ~ 60 nm, while the simulated Hoppel minima are around
468 the size of ~ 100 nm at both sites. This difference in location of Hoppel minima can be
469 attributed to the assumed value of $S=0.5\%$ in the model. The value of S used in the model lies
470 in the range of typical marine stratocumulus clouds, which can vary between 0.1 - 1%
471 (Fossum et al., 2018; Quinn et al., 2017).

472 **3.2 Gas and particle-phase chemical composition of important precursors**

473 Figure 4 shows the simulated gas-phase precursor and main DMS oxidation product
474 concentrations including H₂SO₄, MSA, MSIA, HPMTF, SO₂ and DMSO, for the entire period
475 at the height levels representing Gruebadet (G1 and G2), and Zeppelin (Z1 and Z2). The SO₂
476 gas-phase concentrations are in the order of 10⁶-10⁹ # cm⁻³ (with monthly mean values 1.7 x
477 10⁸ # cm⁻³), which is a factor of 2.3 higher than the average concentrations measured for
478 spring 7.6 x 10⁷ # cm⁻³ by (Lee et al., 2020) at Zeppelin. The monthly mean simulated H₂SO₄
479 gas phase concentrations (6.8 x 10⁵ # cm⁻³) also agree well with the estimated H₂SO₄ proxy
480 (Eq. S1, supplementary) spring average values of 7.5 x 10⁵ # cm⁻³ (Lee et al., 2020) at
481 Zeppelin. Measurements of H₂SO₄ at Gruebadet from May 2017 indicate monthly mean



482 concentrations around $\sim 10^6 \text{ # cm}^{-3}$ (Beck et al., 2021). The modeled H_2SO_4 concentrations at
483 Gruvebadet are $3 \times 10^6 \text{ # cm}^{-3}$, implying a reasonably good model performance in predicting
484 gaseous precursor concentrations. Simulated gas concentrations of MSA ($10^5\text{-}10^8 \text{ # cm}^{-3}$ also
485 agrees well with the measurements made at Gruvebadet in May 2017 by (Beck et al., 2021),
486 wherein they measured daily averages of MSA gas concentrations in the order of 10^7 # cm^{-3} .
487 The low modeled values of MSA and DMSO gas phase concentrations at the height
488 representing Zeppelin (e.g. between 15/05 - 17/05) coincide with the period where the
489 planetary boundary layer height (PBLH) is below the altitude of Zeppelin station (cf. Figure
490 S4 supplementary). Overall, we can conclude that the modeled precursor gas concentrations at
491 the two measurement sites are, in general, good agreement with earlier measurements at the
492 two sites.



494 **Figure 4.** Gas-phase concentrations for the *BaseCase* simulations. The upper two panels (**G1**)
495 and (**Z1**) show the gas-phase concentrations at Gruvebadet and Zeppelin respectively, for
496 compounds H_2SO_4 (red), HIO_3 (gold), MSA (cyan), MSIA (dotted black) and the lower panels
497 (**G2**) and (**Z2**) show the gas-phase concentrations for DMS (blue), HPMTF (orange), SO_2



498 (green) and DMSO (dotted red). Note the different ordinate scales.

499

500 Figure 5 (a) shows the simulated median mass size distribution of compounds Cl^- , Na^+ , MSA,
501 SO_4^{2-} , NH_4^+ , and NO_3^- for the *BaseCase* runs in the lowest model layer. Figure 5(a) indicates
502 that the nucleation mode particles are composed mainly of SO_4^{2-} and NH_4^+ , while MSA, Cl^-
503 and Na^+ dominate PM for larger particles. The observed and modeled high $\text{MSA}_{(\text{g})}$
504 concentrations in comparison to $\text{H}_2\text{SO}_{4(\text{g})}$ at Ny-Ålesund is not reflected in the respective
505 vapor contribution to the nano-particle growth. This is because, in contrast to H_2SO_4 , MSA is
506 not a non-volatile condensable compound. The gas-to-particle partitioning of MSA requires
507 co-condensation and dissolution of (NH_3) (Hodshire et al., 2019) or the existence of cations
508 such as Na^+ which decreases the particle acidity ($[\text{H}^+]$). Figure 5(b) shows the relative mass
509 fraction of the above-mentioned compounds to PM at different sizes. SO_4^{2-} and NH_4^+
510 dominate the mass for particles in the nucleation and Aitken mode. SO_4^{2-} contributes ~74%
511 and ~71% to nucleation and Aitken mode PM, with its contribution decreasing for
512 accumulation (100 nm-1 μm) and coarse (>1 μm) mode PM (~6% and 3.36% respectively)
513 (Table 2). NH_4^+ contribution follows a similar trend, as SO_4^{2-} , with 12.34% and 6.95%
514 contribution to nucleation and Aitken mode PM, but insignificant for accumulation and coarse
515 mode PM (Table 2). The loss of primary sea spray aerosols due to wet scavenging promoted
516 the growth of secondary aerosol particles in the nucleation and Aitken mode by NH_4^+ and
517 SO_4^{2-} as seen in Figure 5 (b). Na^+ (~32.9%), Cl^- (~39.5%) and MSA (20.45%) are the
518 dominant contributors to accumulation and coarse mode PM. In the *BaseCase* simulations,
519 gas-phase SO_2 dissolves in the cloud droplets, and is oxidized by H_2O_2 into SO_4^{2-} (Wollesen
520 de Jonge et al., 2021). Previous modeling studies have shown that a very small fraction of
521 MSA is formed in the gas phase. Instead, most MSA is formed via ozonolysis of MSIA in the
522 aqueous phase (Hoffmann et al., 2016; Wollesen de Jonge et al., 2021). It should be noted that
523 HIO_3 and NO_3^- have an insignificant contribution to total PM_{10} , amounting to ~0.05% and
524 0.17% respectively.

525

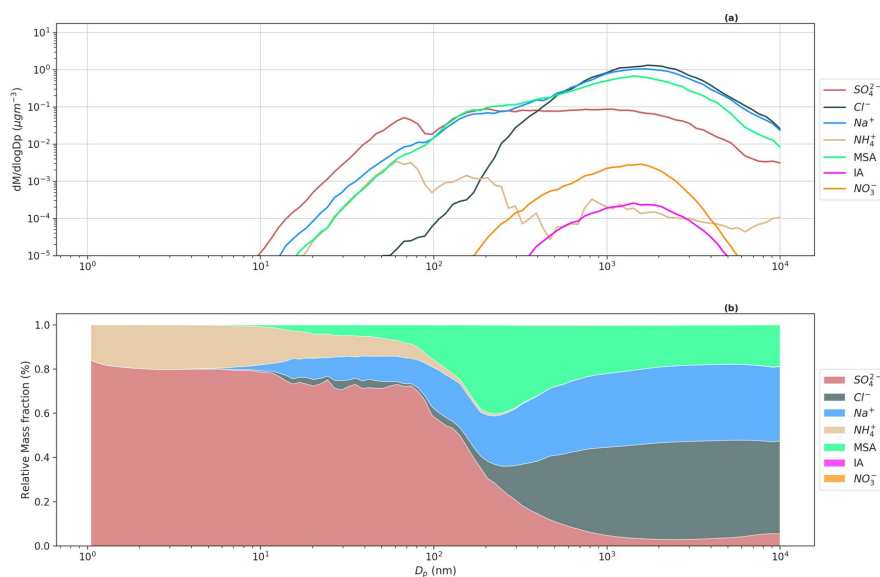
526 **Table 2:** The table shows simulated fractional contribution of different compounds to total
527 PM in different size regimes of nucleation (total $\text{PM}_{<25\text{nm}}$), Aitken (total $\text{PM}_{25-100\text{nm}}$) and
528 accumulation - coarse (total $\text{PM}_{>100\text{nm}}$) mode.

Species	Total	Total Aitken	Total	Total coarse	Total PM_{10}
---------	-------	--------------	-------	--------------	------------------------



	nucleation mode PM fraction (PM _{<25nm}) (%)	mode PM fraction (PM _{25 - 100 nm}) (%)	accumulation mode PM fraction (PM _{100 nm-1 μm}) (%)	mode PM fraction (PM _{>1 μm}) (%)	fractional contribution (%)
SO ₄ ²⁻	73.99	71.00	5.96	3.36	6.67
NH ₄ ⁺	12.34	6.95	0.13	0.06	0.21
Cl ⁻	2.36	1.98	39.96	43.36	39.54
Na ⁺	8.02	11.92	32.90	34.17	32.91
MSA	3.26	8.12	20.58	18.85	20.45
HIO ₃	0.004	0.004	0.05	0.05	0.05
NO ₃ ⁻	0.006	0.01	0.17	0.15	0.17

Median mass size distribution and relative mass fraction (Simulation: BaseCase)



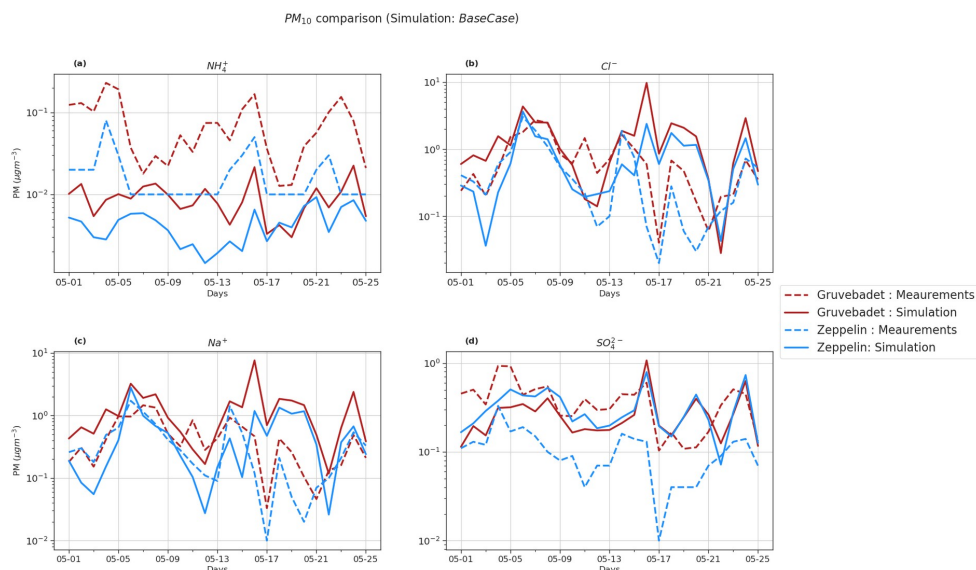
530 **Figure 5.** Simulated median mass size distribution for *BaseCase* simulations. The upper panel
 531 (a) shows the median mass size distribution for compounds Cl⁻, Na⁺, MSA, SO₄²⁻, NH₄⁺, HIO₃
 532 and NO₃⁻ for the entire size distribution ranging from 1.07 nm-10 μm. The lower panel (b)
 533 shows the relative mass fractions or contribution of compounds Cl⁻, Na⁺, MSA, SO₄²⁻, NH₄⁺,
 534 HIO₃ and NO₃⁻ to total non-refractory PM at different sizes.

535 Figure 6 compares the daily PM₁₀ filter measurements to the modeled values at both



536 measurement stations. The model prediction of PM_{10} Cl^- , Na^+ , SO_4^{2-} and NH_4^+ , was evaluated
537 using statistical metrics such as NMB, FAC2, correlation coefficient (r) and RMSE (Table 3).
538 Though the model does well in simulating the trends of PM_{10} SO_4^{2-} , Na^+ and Cl^- at Zeppelin (r
539 values of 0.35, 0.51 and 0.6 respectively), it is unable to predict the NH_4^+ trends accurately (r
540 = -0.08).

541 Pearson correlation (r -values) at Gruvebadet are in the range of 0.29-0.34 for PM_{10} NH_4^+ ,
542 SO_4^{2-} , Na^+ and Cl^- implying that the model trends are reasonably consistent with the measured
543 trends. However, at both Gruvebadet the NMB values for Na^+ and Cl^- are quite large (1.81
544 and 1.05), indicating a large overprediction of the predicted values, while PM_{10} NH_4^+ and
545 SO_4^{2-} at Gruvebadet is underpredicted (NMB = -0.88 and -0.28 respectively). In contrast, at
546 Zeppelin, the modeled PM_{10} SO_4^{2-} is overestimated (NMB=1.96). Likewise, large RMSE and
547 negligible FAC2 values, for PM_{10} Na^+ , and Cl^- imply discrepancies between the predicted and
548 measured values, indicating that the model is overestimating PM_{10} Na^+ and Cl^- at Gruvebadet
549 and PM_{10} SO_4^{2-} at Zeppelin. In summary, the model tends to overpredict PM_{10} Na^+ , Cl^- and
550 SO_4^{2-} concentrations, but on the other hand, does reasonably well in predicting the daily
551 measured trends. Additionally, the modeled PM_{10} Cl^-/Na^+ molar ratio at Gruvebadet and
552 Zeppelin is ~ 0.79 and ~ 0.95 , respectively. This is much higher than the observed PM_{10}
553 Cl^-/Na^+ molar ratio at both sites (~ 0.39). One likely reason for this is the overestimated sea
554 spray aerosol emissions. The PM_{10} Cl^-/Na^+ molar ratios give a measure of the acidic nature of
555 aerosol, since increased condensation of strong acid MSA and H_2SO_4 increases acidity of
556 aerosols thereby causing loss of Cl^- (dechlorination) as HCl (Ayers et al., 1999; Frey et al.,
557 2020). Thus, increased availability of H_2SO_4 and MSA in particle phase in Aitken mode
558 particles results in acid-induced Cl^- loss from sea-spray particles.



560 **Figure 6.** PM₁₀ comparison of *BaseCase* simulations with daily filter samples from
 561 Gruvebadet and Zeppelin for the entire modeled period. Panel (a) shows PM₁₀ NH₄⁺, (b)
 562 shows PM₁₀ Cl⁻, (c) shows PM₁₀ Na⁺ and (d) shows PM₁₀ SO₄²⁻ filter samples. The dotted lines
 563 in each panel indicate measurement values, and the solid line denotes simulated values. The
 564 ordinate is plotted in log scale to better visualize the low values.

565

566 **Table 3:** Evaluation of modeled PM₁₀ values at both sites of Gruvebadet (G) and Zeppelin (Z)
 567 for the four particle-phase species Cl⁻, Na⁺, SO₄²⁻ and NH₄⁺.

Species	Normalized mean bias factor (NMB)	Correlation coefficient (r)	RMSE (µg m ⁻³)	FAC2
NH ₄ ⁺	-0.88 ^G , -0.76 ^Z	0.34 ^G , -0.08 ^Z	0.09 ^G , 0.02 ^Z	0.04 ^G , 0.2 ^Z
Na ⁺	1.81 ^G , 0.36 ^Z	0.29 ^G , 0.51 ^Z	1.67 ^G , 0.55 ^Z	0.4 ^G , 0.48 ^Z
Cl ⁻	1.05 ^G , 0.39 ^Z	0.24 ^G , 0.60 ^Z	2.08 ^G , 0.74 ^Z	0.24 ^G , 0.44 ^Z
SO ₄ ²⁻	-0.28 ^G , 1.96 ^Z	0.33 ^G , 0.35 ^Z	0.27 ^G , 0.26 ^Z	0.6 ^G , 0.24 ^Z

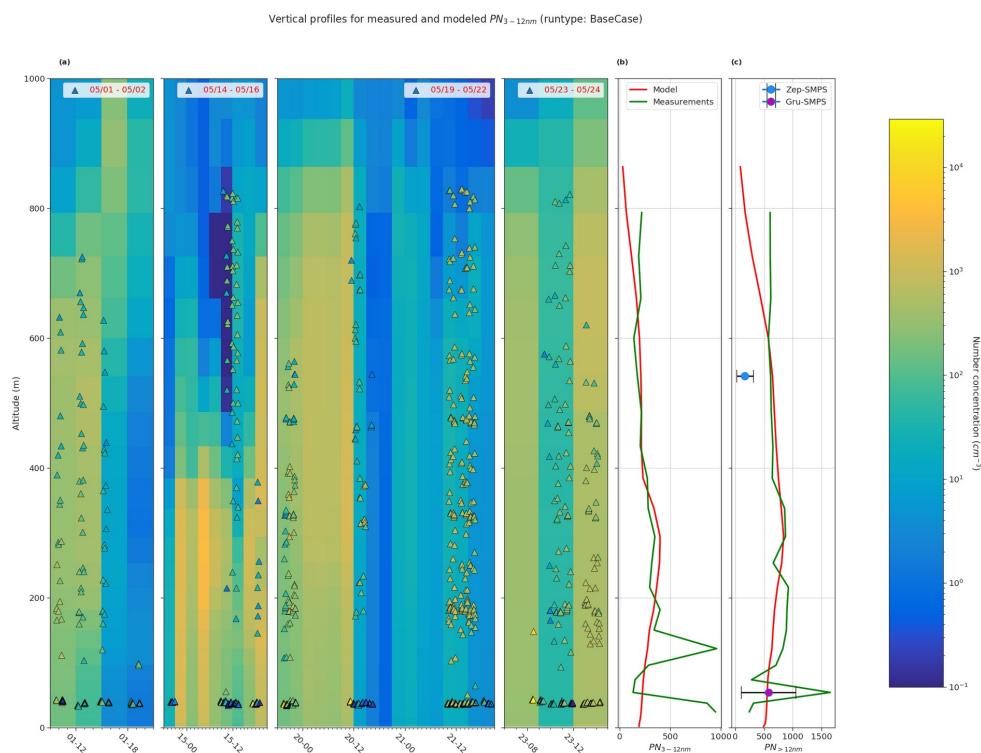
568

569 3.3 Vertical profiles of ultra-fine particle

570 Figure 7 (a) shows the measured vertical PN_{3-12 nm} concentrations from CPC onboard the UAS
 571 for four measurement periods overlayed onto simulated vertical profiles. Figure 7 (b) and (c)



572 show the mean vertical profiles for $PN_{3-12\text{ nm}}$ and $PN_{>12\text{ nm}}$ for both the *BaseCase* simulation and
573 UAS measurements for the entire selected period. The model underestimates the measured
574 $PN_{3-12\text{ nm}}$ and $PN_{>12\text{ nm}}$ vertical particle number concentrations are underestimated by the model
575 below 200 m a.s.l. The NMB for $PN_{3-12\text{ nm}}$ and $PN_{>12\text{ nm}}$ is -0.28 and -0.14, respectively,
576 implying that the model underestimates the particle number concentrations. Both the modeled
577 and measured mean particle number concentrations for $PN_{3-12\text{ nm}}$ and $PN_{>12\text{ nm}}$ are in good
578 agreement between the heights of 200-600 m a.s.l. The lower calculated concentrations of
579 modeled mean particle number concentrations above 600 m a.s.l is most likely affected by
580 higher turbulence in the transition zone from the boundary layer to the free troposphere,
581 which might cause a large mixing of aerosol particles. It should be noted that, at Gruvebadet,
582 the mean SMPS particle number concentrations are in good agreement with the modeled
583 particle number concentrations. However, at the altitude of the Zeppelin station, both the
584 model and UAS measurements of $PN_{>12\text{ nm}}$ are substantially higher (factor of 4) than the mean
585 particle number concentrations measured with the SMPS at Zeppelin. This finding further
586 strengthens the conclusion that the complex orography at Ny-Ålesund highly affects the
587 variability in the vertical scale, which may cause this discrepancy in the observed and
588 modeled particle number concentrations at Zeppelin (see section 3.1). The UAS
589 measurements were carried out at the airport on Ny-Ålesund (and the UAS was flown around
590 Ny-Ålesund) where the boundary layer measurements, like the model, most likely resemble
591 the general Arctic marine boundary layer conditions. Figure S8 shows the influence of
592 different sensitivity simulations on the modeled vertical particle number concentrations. The
593 large spread in the modeled vertical particle number concentrations in Figure S8, highlights
594 the importance of constraining uncertain parameters such as cloud supersaturation and NH_3
595 gas emissions, to better simulate secondary aerosol formation in marine polar regions.



597 **Figure 7.** Comparison of vertical profiles of measured particle number concentration and
598 *BaseCase* simulation. Panel (a) shows measured particle number concentration between 3 -12
599 nm (PN_{3-12nm} , triangles), from CPC onboard the UAS during 4 periods 05/01- 05/02, 05/14 -
600 05/16, 05/19- 05/22, and 05/23- 05/24 (in legend) overlaid onto the simulated PN_{3-12nm} for
601 the same periods. Panel (b) shows the simulated and measured mean PN_{3-12nm} and panel (c)
602 show the $PN_{>12nm}$ for the selected period. Additionally, Panel (c) also shows the mean SMPS
603 particle concentrations at both Gruvebadet and Zeppelin. The horizontal bars for the mean
604 SMPS values represent the standard deviation.

605

606 3.4 Sensitivity Tests

607 In this section, we will discuss the results from the sensitivity tests that we performed to
608 complement the main *BaseCase* simulations.

609 Median particle size distribution for sensitivity tests

610 The sensitivity study *Cloudoff* was performed to test how in-cloud processing affects the

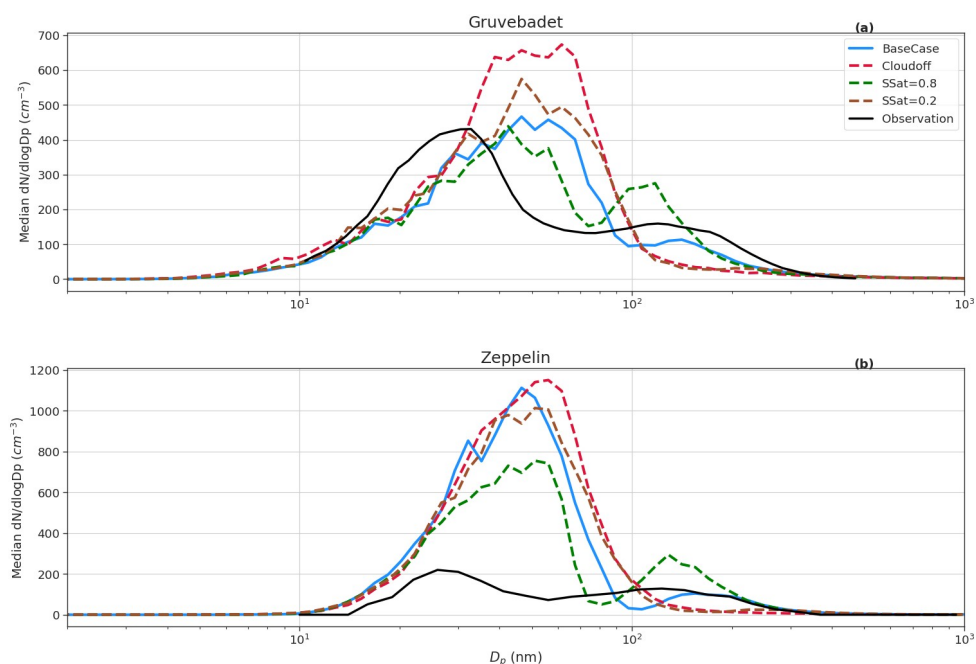


611 formation of larger particles, especially the accumulation mode (Figure 8). In the *Cloudoff*
612 test, in-cloud processing was switched off in the model and the RH was set to just below
613 supersaturation (99.9999%) in the model grid cell where clouds (RH=100.5%) exists in the
614 *BaseCase* runs. The aim of the *Cloudoff* simulation was to investigate if the model can
615 capture the observed accumulation mode without aerosol cloud processing. It is clear from
616 Figure 8 (a) and (b) that in *Cloudoff* simulations, the median size distribution lacks the
617 accumulation mode and Hoppel minima and has a higher Aitken mode particle concentration
618 compared to either *BaseCase* or the measured median size distribution. This further
619 emphasizes the importance of in-cloud processing in activation of particles to CCN sizes and
620 their growth to larger sizes. Another noteworthy point in *Cloudoff* simulations is the larger
621 number concentration of particles <10 nm compared to other cases. One plausible reason is
622 the lack of activated cloud droplets, since the large surface areas of activated droplets are
623 efficient at Brownian scavenging of smaller particles (Hudson et al., 2015). Likewise, the
624 median particle number size distribution from the sensitivity tests with lower cloud
625 supersaturation (S) of 0.2% $SSat=0.2$, reduces the accumulation mode particles, since there
626 are fewer particles with $S_c < S$ available for activation. Increasing S to 0.8% increases
627 accumulation mode particles, since more particles with $S_c < S$ are activated to cloud droplets
628 (Aitken mode concentration decreases with respect to *BaseCase* simulations, since more
629 smaller particles are activated into cloud droplets). Therefore, simulated results show that
630 increasing the cloud supersaturation results in a higher number of smaller particles being
631 activated into cloud droplets and shifts the simulated Hoppel minima close to the measured
632 sizes. Figure S5, in supplementary shows median particle size distribution for all sensitivity
633 tests.

634 The *SalterSSA* sensitivity test underestimates both the Aitken and accumulation mode
635 concentrations at Gruebadet (Figure S5, supplementary). The Salter sea-spray
636 parameterization produces ~ 2 magnitudes fewer Aitken mode particles compared to Sofiev
637 et. al, 2011, while the coarse mode particle emissions using *SalterSSA* parameterization are
638 higher than Sofiev et. al 2011. This can cause MSA, H_2SO_4 and NH_3 to partition onto coarse
639 mode particles rather than contributing to NPF and growth of the nucleation and Aitken mode
640 particles, which substantially lowers the Aitken and accumulation mode number
641 concentrations. The *NPFoff* simulation from Figure S5 shows lower Aitken mode
642 concentrations, implying that the main contributor to Aitken mode particle number
643 concentrations are the secondary aerosols rather than the primary sea-salt particles.



27



645 **Figure 8:** Median size distribution at Gruvebadet (panel (a)) and Zeppelin (panel (b)) for all
646 the sensitivity tests *Cloudoff*, *SSat=0.8*, and *SSat=0.2* (colored dashed lines) including
647 *BaseCase* (blue solid line) and observations (black solid line).

648 Another parameter of uncertainty is the concentration of NH_3 in the marine atmosphere. The
649 *LowNH₃* simulations, as expected, result in lower Aitken mode particles, whereas *HighNH₃*
650 simulations show an overprediction of Aitken mode concentrations (Figure S5,
651 supplementary). This underlines the necessity of constraining ocean and marine emissions of
652 NH_3 to better predict the aerosol particle formation in marine polar environments.

653 Particle phase comparison for sensitivity tests

654 Figure 9 shows the contribution of constituent compounds to PM at different particle sizes
655 with respect to the *BaseCase* simulation. The overall mean contribution of SO_4^{2-} and MSA to
656 total PM_{10} decreased by $\sim 8\%$ and 11% respectively, in *Cloudoff* runs compared to the
657 *BaseCase* simulations. It is expected that in non-cloud conditions there is a reduction in SO_4^{2-}
658 and MSA PM contribution because of the reduced partitioning of gaseous SO_2 to the cloud
659 droplets (for PM SO_4^{2-} formation) and inhibition of MSIA ozonolysis in the cloud droplets
660 (leading to PM MSA formation) (Chen et al., 2018; Hoffmann et al., 2016; Wollesen de Jonge
661 et al., 2021). This is observed for accumulation mode particles between size ranges of 100 nm

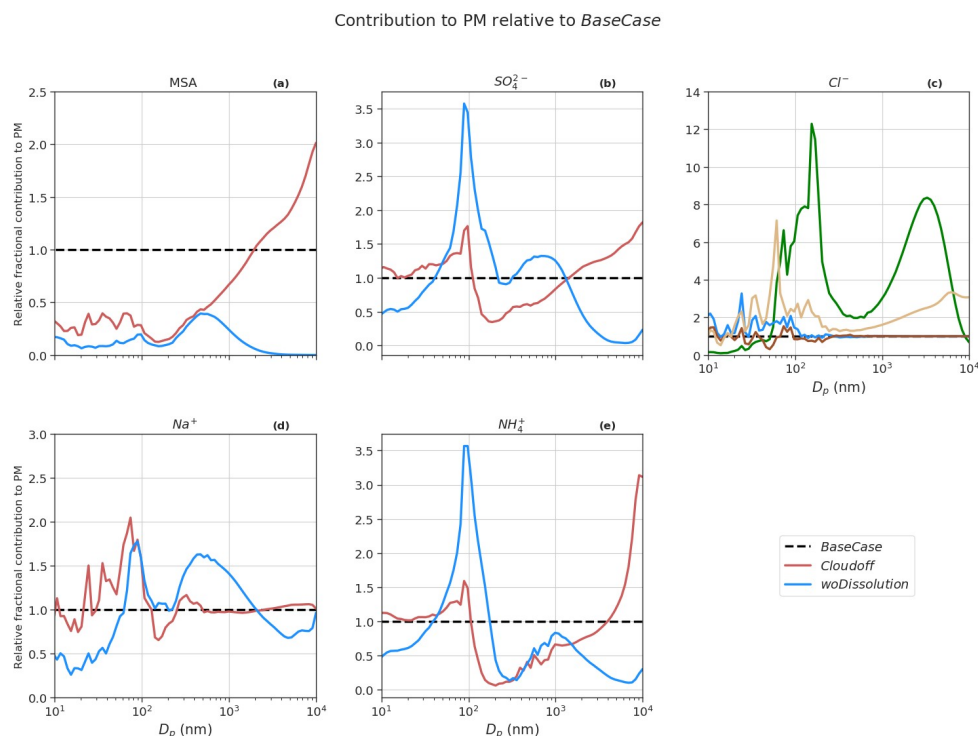


662 to 1 μm which is characterized by lower SO_4^{2-} and MSA PM. On the other hand, PM SO_4^{2-} and
663 MSA increase for coarse mode particles ($> 1 \mu\text{m}$). Without cloud droplet activation the
664 deliquescent sea spray coarse mode particles become a major liquid water reservoir where
665 MSIA and to a lesser extent SO_2 are dissolved and oxidized into MSA and SO_4^{2-} , which partly
666 explains the increase in PM MSA and SO_4^{2-} for sizes $> 1 \mu\text{m}$. The results from *Cloudoff*
667 simulation agrees with the findings from Wollesen de Jonge et al., 2021, who found that MSA
668 was almost exclusively formed in the aqueous phase via MSIA ozonolysis in cloud droplets
669 and deliquescent particles during and in between in-cloud periods. PM SO_4^{2-} in *Cloudoff* runs
670 is mainly driven via condensation of H_2SO_4 , since an increase in SO_2 gas-phase
671 concentrations ($\sim 42\%$ with respect to *BaseCase*) promoted gas-phase H_2SO_4 production
672 (increase of $\sim 44\%$ with respect to *BaseCase*), and therefore H_2SO_4 derived PM SO_4^{2-} .

673 In the *woDissolution* simulation, all the PM MSA and SO_4^{2-} are a result of the condensation of
674 $\text{MSA}_{(\text{g})}$ and $\text{H}_2\text{SO}_{4(\text{g})}$, since irreversible aqueous-phase chemistry is switched off. The overall
675 contribution of PM SO_4^{2-} to the total PM_{10} increases by $\sim 12\%$ relative to the *BaseCase* run,
676 while on the other hand, the contribution of PM MSA decreases by $\sim 87\%$ (relative to
677 *BaseCase*). The lower PM_{10} MSA in *woDissolution* simulation emphasizes the importance of
678 aqueous-phase formation of MSA to the growth of particles. The effect of precipitation on
679 modeled PM (*NoPrecip*) indicates an increase in PM Na^+ and Cl^- of $\sim 112\%$ and 119%
680 respectively, as compared to *BaseCase* (Figure S7). This is because of the decrease in the wet
681 deposition of aerosol and sea-spray particles by rain events and below cloud scavenging. The
682 consequence of neglecting precipitation results in increased condensation sink for H_2SO_4 and
683 NH_3 (increase of 62% and 22% in PM SO_4^{2-} , NH_4^+ respectively), but since sea-spray aerosols
684 are not scavenged by the wet removal process, the overall fractional contribution to PM by
685 SO_4^{2-} , NH_4^+ and MSA is lower relative to *BaseCase* runs.

686 *SalterSSA* simulation results in higher PM Cl^- and Na^+ (470% and 371% increase respectively)
687 compared to *BaseCase* runs. This is because Salter15 SSA parameterization produces larger
688 mass emission fluxes in size ranges $> 1 \mu\text{m}$ compared to Sofiev11 SSA parameterization
689 (Barthel et al., 2019). Additionally, there is an increase of $\sim 19\%$ in PM MSA, largely due to
690 formation of MSA in larger deliquescent coarse mode particles.

691



692 **Figure 9:** Contribution of constituent compounds, namely, MSA (panel (a)), SO_4^{2-} (panel (b)),
693 Cl^- (panel(c)), Na^+ (panel (d)) and NH_4^+ (panel (e)) to PM with respect to *BaseCase* (the black
694 dotted line).

695 4. Summary and conclusions

696 In this work, we attempt to simulate secondary aerosol formation at remote Arctic sites of
697 Gruvebadat and Zeppelin, Ny-Ålesund, during the period of 1st - 25th of May 2018. We used
698 the 1-dimensional column model ADCHEM which was run along FLEXPART generated
699 Lagrangian trajectories. Since the air mass spend most of their time over the open ocean
700 upwind of Ny-Ålesund, we use a comprehensive multi-phase DMS chemistry scheme coupled
701 with MCMv3.3.1 and PRAM.

702 In the model, new particles are formed via ion-mediated $H_2SO_4-NH_3$ nucleation, with the
703 initial particle growth mainly driven by condensation of H_2SO_4 , while the secondary PM_{10}
704 MSA and SO_4^{2-} contribution was mainly formed by oxidation of MSIA and SO_2 in the
705 aqueous phase. At Gruvebadet, the modeled median particle number size distribution agrees
706 reasonably well with the measurements, however, at Zeppelin, the simulated Aitken mode
707 median concentration is overestimated by a factor of 5.5. This relatively large discrepancy in



708 modeled and measured particle size distributions at Zeppelin, and likewise the large
709 difference between the measured particle number size distributions at Gruvebadet and
710 Zeppelin, can to a large extent be explained by the orographic effects at Zeppelin which
711 distorts the atmospheric boundary layer dynamics. Thus, while the model generally is able to
712 capture the particle number size distribution dynamics in the marine boundary layer, as
713 measured at the near sea level Gruvebadet site, it generally cannot capture the observations at
714 the mountain station of Zeppelin, which often lies above the boundary layer and may
715 experience free tropospheric conditions. This is also supported by the fact that $PN_{>12\text{ nm}}$
716 concentrations measured with the UAS above Ny-Ålesund airport agrees well with the
717 modeled particle number concentrations, at the same altitude as Zeppelin. However, both the
718 model and UAS $PN_{>12\text{ nm}}$ concentrations is a factor of 4 higher than the $PN_{>12\text{ nm}}$ observation at
719 Zeppelin.

720 Both the measured and modeled particle size distribution, at both stations, show a distinct
721 Hoppel minima, which can be explained by tin-cloud processing. Model sensitivity runs with
722 varying cloud supersaturation indicate that a cloud supersaturation of 0.5% or higher is
723 required for the model to capture the observed Hoppel minima. Furthermore, model
724 sensitivity runs show that the Aitken mode particle number concentrations are dominated by
725 contribution of secondary aerosols rather than primary emissions. The modeled PM_{10} Cl^- and
726 Na^+ is positively correlated when compared to PM_{10} filter samples. The main driver for
727 secondary aerosol particle growth is the formation of MSA via aqueous phase ozonolysis of
728 the DMS oxidation product MSIA. This demonstrates the importance of multi-phase DMS
729 chemistry in capturing the size resolved secondary aerosol growth in marine polar regions.

730 The sensitivity studies indicate that it is important to limit the uncertainties in parameters such
731 as cloud supersaturation and NH_3 emissions over open oceans to get a better constraint on
732 secondary aerosol formation and its subsequent climatic effects. This work was a first attempt
733 to simulate new particle and secondary aerosol formation in marine polar regions using a
734 process based chemistry transport model that includes a comprehensive multi-phase DMS and
735 halogen chemistry mechanism, detailed gas-molecular cluster and aerosol dynamics. In future
736 studies, we aim to implement ADCHEM for extended studies in polar marine and remote
737 continental regions where different atmospheric constituents such as HIO_3 , terpenes and
738 amines drive secondary aerosol formation.

739 **Acknowledgments**

740 The ALADINA study was funded by the German Research Foundation under grants LA



741 2907/5-3 and WI 1449/22-3. M. Sipilä acknowledges Academy of Finland (296628) and the
742 European Research Council (ERC) under the European Union's Horizon 2020 research and
743 innovation programme (GASPARCON, grant agreement no. 714621). This project has
744 received funding from the Swedish Research Council Formas project no. 2018-01745-
745 COBACCA, Swedish Research Council VR project no. 2019-05006, the Crafoord foundation
746 through project number 20210969. The presented research has been also been funded by the
747 Academy of Finland (Center of Excellence in Atmospheric Sciences) grant no. 4100200.
748 The authors would like to thank Tinja Olenius from the Swedish Meteorological and
749 Hydrological (SMHI) for help with the implementation of ACDC in ADCHEM. We would
750 also like to acknowledge the invaluable contribution of computational resources from CSC-IT
751 Center for Science, Finland. The authors would like to thank Noora Hyytinen from the
752 University of Oulu and University of Eastern Finland for providing the Henry's law
753 coefficient and dissolution constants which were used in the multi-phase chemistry.

754

755 **Author Contributions**

756 CX, PR, MBoy, BA and BW planned and designed the study. PR, RWdJ and CX developed
757 and setup the ADCHEM model. CX, MB and VV performed the FLEXPART model
758 simulations. BA, BW, RoTh, and RT provided the measurement data. Resources were
759 provided by PR and MBoy. CX, PR and MBoy wrote the original draft, which included
760 visualizations made by CX and PR. All other authors discussed the results and contributed to
761 the final manuscript.

762

763 **Competing interests**

764 The authors declare that they do have no conflict of interest.

765 **References**

766 AMAP: Snow, Water, Ice and Permafrost in the Arctic (SWIPA): Climate Change and the
767 Cryosphere. [online] Available from:
768 <http://amap.no/swipa/><http://amap.no/swipa/CombinedReport.pdf><http://amap.no/swipa/SWIPA2011ExecutiveSummaryV2.pdf><http://amap.no/swipa/SwipaSimpleSummary-SEC.pdf>, 2011.
770
771 AMAP: AMAP, 2017. Snow, Water, Ice and Permafrost in the Arctic (SWIPA) 2017. Arctic
772 Monitoring and Assessment Programme (AMAP), Oslo, Norway. xiv + 269 pp. [online]
773 Available from: <https://www.amap.no/documents/doc/snow-water-ice-and-permafrost-in-the->



- 774 arctic-swipa-2017/1610, 2017.
- 775 Amore, A., Giardi, F., Becagli, S., Caiazzo, L., Mazzola, M., Severi, M. and Traversi, R.:
776 Source apportionment of sulphate in the High Arctic by a 10 yr-long record from Gruevbadet
777 Observatory (Ny-Ålesund, Svalbard Islands), *Atmos. Environ.*, 270(July 2021),
778 doi:10.1016/j.atmosenv.2021.118890, 2022.
- 779 Arrigo, K. R. and van Dijken, G. L.: Continued increases in Arctic Ocean primary production,
780 *Prog. Oceanogr.*, 136, 60–70, doi:10.1016/j.pocean.2015.05.002, 2015.
- 781 Ayers, G. P., Gillett, R. W., Caaney, J. M. and Dick, A. L.: Chloride and bromide loss from
782 sea-salt particles in Southern Ocean air, *J. Atmos. Chem.*, 33(3), 299–319,
783 doi:10.1023/A:1006120205159, 1999.
- 784 Baccarini, A., Karlsson, L., Dommen, J., Duplessis, P., Vüllers, J., Brooks, I. M., Saiz-Lopez,
785 A., Salter, M., Tjernström, M., Baltensperger, U., Zieger, P. and Schmale, J.: Frequent new
786 particle formation over the high Arctic pack ice by enhanced iodine emissions, *Nat.*
787 *Commun.*, 11(1), 1–11, doi:10.1038/s41467-020-18551-0, 2020.
- 788 Bärffuss, K., Pätzold, F., Altstädter, B., Kathe, E., Nowak, S., Bretschneider, L., Bestmann, U.
789 and Lampert, A.: New setup of the UAS ALADINA for measuring boundary layer properties,
790 atmospheric particles and solar radiation, *Atmosphere (Basel)*, 9(1),
791 doi:10.3390/atmos9010028, 2018.
- 792 Barnes, I., Hjorth, J. and Mihalopoulos, N.: Dimethyl sulfide and dimethyl sulfoxide and their
793 oxidation in the atmosphere, *Chem. Rev.*, 106(3), 940–975, doi:10.1021/cr020529+, 2006.
- 794 Barrie, L. A.: Arctic air pollution: An overview of current knowledge, *Atmos. Environ.*,
795 20(4), 643–663, doi:10.1016/0004-6981(86)90180-0, 1986.
- 796 Barthel, S., Tegen, I. and Wolke, R.: Do new sea spray aerosol source functions improve the
797 results of a regional aerosol model?, 2019.
- 798 Beck, L. J., Sarnela, N., Junninen, H., Hoppe, C. J. M., Garmash, O., Bianchi, F., Riva, M.,
799 Rose, C., Peräkylä, O., Wimmer, D., Kausiala, O., Jokinen, T., Ahonen, L., Mikkilä, J.,
800 Hakala, J., He, X. C., Kontkanen, J., Wolf, K. K. E., Cappelletti, D., Mazzola, M., Traversi,
801 R., Petroselli, C., Viola, A. P., Vitale, V., Lange, R., Massling, A., Nøjgaard, J. K., Krejci, R.,
802 Karlsson, L., Zieger, P., Jang, S., Lee, K., Vakkari, V., Lampilahti, J., Thakur, R. C., Leino,
803 K., Kangasluoma, J., Duplissy, E. M., Siivola, E., Marbouti, M., Tham, Y. J., Saiz-Lopez, A.,
804 Petäjä, T., Ehn, M., Worsnop, D. R., Skov, H., Kulmala, M., Kerminen, V. M. and Sipilä, M.:
805 Differing Mechanisms of New Particle Formation at Two Arctic Sites, *Geophys. Res. Lett.*,
806 48(4), 1–11, doi:10.1029/2020GL091334, 2021.
- 807 Bengtsson, L., Hodges, K. I., Koumoutsaris, S., Zahn, M. and Berrisford, P.: The changing
808 energy balance of the polar regions in a warmer climate, *J. Clim.*, 26(10), 3112–3129,
809 doi:10.1175/JCLI-D-12-00233.1, 2013.
- 810 Berndt, T., Chen, J., Møller, K. H., Hyttinen, N., Prisle, N. L., Tilgner, A., Hoffmann, E. H.,
811 Herrmann, H. and Kjaergaard, H. G.: SO₂ formation and peroxy radical isomerization in the



- 812 atmospheric reaction of OH radicals with dimethyl disulfide, *Chem. Commun.*, 56(88),
813 13634–13637, doi:10.1039/d0cc05783e, 2020.
- 814 Bräuer, P., Tilgner, A., Wolke, R. and Herrmann, H.: Mechanism development and modelling
815 of tropospheric multiphase halogen chemistry: The CAPRAM Halogen Module 2.0 (HM2), *J.*
816 *Atmos. Chem.*, 70(1), 19–52, doi:10.1007/s10874-013-9249-6, 2013.
- 817 Campolongo, F., Saltelli, A., Jensen, N. R., Wilson, J. and Hjorth, J.: The role of multiphase
818 chemistry in the oxidation of dimethylsulphide (DMS). A latitude dependent analysis, *J.*
819 *Atmos. Chem.*, 32(3), 327–356, doi:10.1023/A:1006154618511, 1999.
- 820 Chen, Q., Sherwen, T., Evans, M. and Alexander, B.: DMS oxidation and sulfur aerosol
821 formation in the marine troposphere: A focus on reactive halogen and multiphase chemistry,
822 *Atmos. Chem. Phys.*, 18(18), 13617–13637, doi:10.5194/acp-18-13617-2018, 2018.
- 823 Clarke, A. D., Owens, S. R. and Zhou, J.: An ultrafine sea-salt flux from breaking waves:
824 Implications for cloud condensation nuclei in the remote marine atmosphere, *J. Geophys. Res.*
825 *Atmos.*, 111(6), doi:10.1029/2005JD006565, 2006.
- 826 Cuevas, C. A., Maffezzoli, N., Corella, J. P., Spolaor, A., Vallelonga, P., Kjær, H. A.,
827 Simonsen, M., Winstrup, M., Vinther, B., Horvat, C., Fernandez, R. P., Kinnison, D.,
828 Lamarque, J. F., Barbante, C. and Saiz-Lopez, A.: Rapid increase in atmospheric iodine levels
829 in the North Atlantic since the mid-20th century, *Nat. Commun.*, 9(1), 1–6,
830 doi:10.1038/s41467-018-03756-1, 2018.
- 831 Dall’osto, M., Beddows, D. C. S., Tunved, P., Harrison, R. M., Lupi, A., Vitale, V., Becagli,
832 S., Traversi, R., Park, K. T., Jun Yoon, Y., Massling, A., Skov, H., Lange, R., Strom, J. and
833 Krejci, R.: Simultaneous measurements of aerosol size distributions at three sites in the
834 European high Arctic, *Atmos. Chem. Phys.*, 19(11), 7377–7395, doi:10.5194/acp-19-7377-
835 2019, 2019.
- 836 Dall’Osto, M., Ovadnevaite, J., Paglione, M., Beddows, D. C. S., Ceburnis, D., Cree, C.,
837 Cortés, P., Zamanillo, M., Nunes, S. O., Pérez, G. L., Ortega-Retuerta, E., Emelianov, M.,
838 Vaqué, D., Marrasé, C., Estrada, M., Sala, M. M., Vidal, M., Fitzsimons, M. F., Beale, R.,
839 Airs, R., Rinaldi, M., Decesari, S., Facchini, M. C., Harrison, R. M., O’Dowd, C. and Simó,
840 R.: Antarctic sea ice region as a source of biogenic organic nitrogen in aerosols, *Sci. Rep.*,
841 7(1), 1–10, doi:10.1038/s41598-017-06188-x, 2017.
- 842 Dall’Osto, M., Beddows, D. C. S., Tunved, P., Harrison, R. M., Lupi, A., Vitale, V., Becagli,
843 S., Traversi, R., Park, K.-T., Yoon, Y. J., Massling, A., Skov, H., Lange, R., Strom, J. and
844 Krejci, R.: Simultaneous measurements of aerosol size distributions at three sites in the
845 European high Arctic, *Atmos. Chem. Phys.*, 19(11), 7377–7395, doi:10.5194/acp-19-7377-
846 2019, 2019.
- 847 Dall’osto, M., Beddows, D. C. S., Tunved, P., Krejci, R., Ström, J., Hansson, H. C., Yoon, Y.
848 J., Park, K. T., Becagli, S., Udisti, R., Onasch, T., Ódowd, C. D., Simó, R. and Harrison, R.
849 M.: Arctic sea ice melt leads to atmospheric new particle formation, *Sci. Rep.*, 7(1), 1–10,
850 doi:10.1038/s41598-017-03328-1, 2017.



- 851 Damian, V., Sandu, A., Damian, M., Potra, F. and Carmichael, G. R.: The kinetic
852 preprocessor KPP - A software environment for solving chemical kinetics, *Comput. Chem.*
853 *Eng.*, 26(11), 1567–1579, doi:10.1016/S0098-1354(02)00128-X, 2002.
- 854 Feingold, G. and Kreidenweis, S.: Does cloud processing of aerosol enhance droplet
855 concentrations?, *J. Geophys. Res. Atmos.*, 105(D19), 24351–24361,
856 doi:10.1029/2000JD900369, 2000.
- 857 Flossmann, A. I. and Wobrock, W.: Cloud processing of aerosol particles in marine
858 stratocumulus clouds, *Atmosphere (Basel)*., 10(9), doi:10.3390/atmos10090520, 2019.
- 859 Fossum, K. N., Ovadnevaite, J., Ceburnis, D., Dall’Osto, M., Marullo, S., Bellacicco, M.,
860 Simó, R., Liu, D., Flynn, M., Zuend, A. and O’Dowd, C.: Summertime Primary and
861 Secondary Contributions to Southern Ocean Cloud Condensation Nuclei, *Sci. Rep.*, 8(1), 1–
862 14, doi:10.1038/s41598-018-32047-4, 2018.
- 863 Frey, M. M., Norris, S. J., Brooks, I. M., Anderson, P. S., Nishimura, K., Yang, X., Jones, A.
864 E., Nerentorp Mastromonaco, M. G., Jones, D. H. and Wolff, E. W.: First direct observation
865 of sea salt aerosol production from blowing snow above sea ice, *Atmos. Chem. Phys.*, 20(4),
866 2549–2578, doi:10.5194/acp-20-2549-2020, 2020.
- 867 Gantt, B., He, J., Zhang, X., Zhang, Y. and Nenes, A.: Incorporation of advanced aerosol
868 activation treatments into CESM/CAM5: Model evaluation and impacts on aerosol indirect
869 effects, *Atmos. Chem. Phys.*, 14(14), 7485–7497, doi:10.5194/acp-14-7485-2014, 2014.
- 870 Granier, C., Darras, S., Gon, H. D. van der, Jana, D., Elguindi, N., Bo, G., Michael, G., Marc,
871 G., Jalkanen, J.-P., Kuenen, J., Liousse, C., Quack, B., Simpson, D. and Sindelarova, K.: The
872 Copernicus Atmosphere Monitoring Service global and regional emissions (April 2019
873 version), (April) [online] Available from: [https://hal.archives-ouvertes.fr/hal-](https://hal.archives-ouvertes.fr/hal-02322431)
874 [02322431%0Ahttps://hal.archives-ouvertes.fr/hal-02322431/document](https://hal.archives-ouvertes.fr/hal-02322431/document), 2019.
- 875 Guenther, A., Karl, T., Harley, P., Weidinmyer, C., Palmer, P. I. and Geron, C.: Edinburgh
876 Research Explorer Estimates of global terrestrial isoprene emissions using MEGAN (Model
877 of Emissions of Gases and Aerosols from Nature) and Physics Estimates of global terrestrial
878 isoprene emissions using MEGAN (Model of Emissions of Gases an, *Atmos. Chem. Phys.*,
879 (6), 3181–3210, 2006.
- 880 Herenz, P., Wex, H., Henning, S., Kristensen, T. B., Rubach, F., Roth, A., Borrmann, S.,
881 Bozem, H., Schulz, H. and Stratmann, F.: Measurements of aerosol and CCN properties in the
882 Mackenzie River delta (Canadian Arctic) during spring--summer transition in May 2014,
883 *Atmos. Chem. Phys.*, 18(7), 4477–4496, doi:10.5194/acp-18-4477-2018, 2018.
- 884 Hertel, O., Christensen, J. and Hov, Ø.: Modelling of the end products of the chemical
885 decomposition of DMS in the marine boundary layer, *Atmos. Environ.*, 28(15), 2431–2449,
886 doi:10.1016/1352-2310(94)90395-6, 1994.
- 887 Hodshire, A. L., Campuzano-Jost, P., Kodros, J. K., Croft, B., Nault, B. A., Schroder, J. C.,
888 Jimenez, J. L. and Pierce, J. R.: The potential role of methanesulfonic acid (MSA) in aerosol
889 formation and growth and the associated radiative forcings, *Atmos. Chem. Phys.*, 19(5),



- 890 3137–3160, doi:10.5194/acp-19-3137-2019, 2019.
- 891 Hoffmann, E. H., Tilgner, A., Schrödner, R., Bräuer, P., Wolke, R. and Herrmann, H.: An
892 advanced modeling study on the impacts and atmospheric implications of multiphase
893 dimethyl sulfide chemistry, *Proc. Natl. Acad. Sci. U. S. A.*, 113(42), 11776–11781,
894 doi:10.1073/pnas.1606320113, 2016.
- 895 Hoose, C., Lohmann, U., Bennartz, R., Croft, B. and Lesins, G.: Global simulations of aerosol
896 processing in clouds, *Atmos. Chem. Phys.*, 8(23), 6939–6963, doi:10.5194/acp-8-6939-2008,
897 2008.
- 898 Hoppel, W. A. and Frick, G. M.: Submicron aerosol size distributions measured over the
899 tropical and South Pacific, *Atmos. Environ. Part A, Gen. Top.*, 24(3), 645–659,
900 doi:10.1016/0960-1686(90)90020-N, 1990.
- 901 Hoppel, W. A., Fitzgerald, J. W. and Larson, R. E.: Aerosol size distributions in air masses
902 advecting off the east coast of the United States., *J. Geophys. Res.*, 90(D1), 2365–2379,
903 doi:10.1029/JD090iD01p02365, 1985.
- 904 Hoppel, W. A., Frick, G. M. and Larson, R. E.: Effect of nonprecipitating clouds on the
905 aerosol size distribution in the marine boundary layer, *Geophys. Res. Lett.*, 13, 125–128,
906 1986.
- 907 Hudson, J. G., Noble, S. and Tabor, S.: Cloud supersaturations from CCN spectra Hoppel
908 minima, *J. Geophys. Res.*, 120(8), 3436–3452, doi:10.1002/2014JD022669, 2015.
- 909 Jenkin, M. E., Saunders, S. M. and Pilling, M. J.: The tropospheric degradation of volatile
910 organic compounds: A protocol for mechanism development, *Atmos. Environ.*, 31(1), 81–
911 104, doi:10.1016/S1352-2310(96)00105-7, 1997.
- 912 Jenkin, M. E., Young, J. C. and Rickard, A. R.: The MCM v3.3.1 degradation scheme for
913 isoprene, *Atmos. Chem. Phys.*, 15(20), 11433–11459, doi:10.5194/acp-15-11433-2015, 2015.
- 914 Jeričević, A., Kraljević, L., Grisogono, B., Fagerli, H. and Večenaj, Ž.: Parameterization of
915 vertical diffusion and the atmospheric boundary layer height determination in the EMEP
916 model, *Atmos. Chem. Phys.*, 10(2), 341–364, doi:10.5194/acp-10-341-2010, 2010.
- 917 Jokinen, T., Sipilä, M., Kontkanen, J., Vakkari, V., Tisler, P., Duplissy, E. M., Junninen, H.,
918 Kangasluoma, J., Manninen, H. E., Petäjä, T., Kulmala, M., Worsnop, D. R., Kirkby, J.,
919 Virkkula, A. and Kerminen, V. M.: Ion-induced sulfuric acid–ammonia nucleation drives
920 particle formation in coastal Antarctica, *Sci. Adv.*, 4(11), 1–7, doi:10.1126/sciadv.aat9744,
921 2018.
- 922 Kettle, A. J. and Andreae, M. O.: Flux of dimethylsulfide from the oceans: A comparison of
923 updated data sets and flux models, *J. Geophys. Res. Atmos.*, 105(D22), 26793–26808,
924 doi:10.1029/2000JD900252, 2000.
- 925 Kim, I., Zhang, M., Kim, K. and Park, K.: First high-frequency underway observation of dms
926 distribution in the southern ocean during austral autumn, *Atmosphere (Basel)*, 12(1), 1–10,
927 doi:10.3390/atmos12010122, 2021.



- 928 Kirkby, J., Duplissy, J., Sengupta, K., Frege, C., Gordon, H., Williamson, C., Heinritzi, M.,
929 Simon, M., Yan, C., Almeida, J., Trostl, J., Nieminen, T., Ortega, I. K., Wagner, R., Adamov,
930 A., Amorim, A., Bernhammer, A. K., Bianchi, F., Breitenlechner, M., Brilke, S., Chen, X.,
931 Craven, J., Dias, A., Ehrhart, S., Flagan, R. C., Franchin, A., Fuchs, C., Guida, R., Hakala, J.,
932 Hoyle, C. R., Jokinen, T., Junninen, H., Kangasluoma, J., Kim, J., Krapf, M., Kurten, A.,
933 Laaksonen, A., Lehtipalo, K., Makhmutov, V., Mathot, S., Molteni, U., Onnela, A., Perakyla,
934 O., Piel, F., Petaja, T., Praplan, A. P., Pringle, K., Rap, A., Richards, N. A. D., Riipinen, I.,
935 Rissanen, M. P., Rondo, L., Sarnela, N., Schobesberger, S., Scott, C. E., Seinfeld, J. H.,
936 Sipila, M., Steiner, G., Stozhkov, Y., Stratmann, F., Tomé, A., Virtanen, A., Vogel, A. L.,
937 Wagner, A. C., Wagner, P. E., Weingartner, E., Wimmer, D., Winkler, P. M., Ye, P., Zhang,
938 X., Hansel, A., Dommen, J., Donahue, N. M., Worsnop, D. R., Baltensperger, U., Kulmala,
939 M., Carslaw, K. S. and Curtius, J.: Ion-induced nucleation of pure biogenic particles, *Nature*,
940 533(7604), 521–526, doi:10.1038/nature17953, 2016.
- 941 Kloster, S., Feichter, J., Maier-Reimer, E., Six, K. D., Stier, P. and Wetzel, P.: DMS cycle in
942 the marine ocean-atmosphere system - A global model study, *Biogeosciences*, 3(1), 29–51,
943 doi:10.5194/bg-3-29-2006, 2006.
- 944 Lampert, A., Altstädter, B., Bärfuss, K., Bretschneider, L., Sandgaard, J., Michaelis, J.,
945 Lobitz, L., Asmussen, M., Damm, E., Käthner, R., Krüger, T., Lüpkes, C., Nowak, S., Peucker,
946 A., Rausch, T., Reiser, F., Scholtz, A., Sotomayor-Zakharov, D., Gaus, D., Bansmer, S.,
947 Wehner, B. and Pätzold, F.: Unmanned aerial systems for investigating the polar atmospheric
948 boundary layer-technical challenges and examples of applications, *Atmosphere (Basel)*,
949 11(4), doi:10.3390/ATMOS11040416, 2020.
- 950 Lana, A., Bell, T. G., Simó, R., Vallina, S. M., Ballabrera-Poy, J., Kettle, A. J., Dachs, J.,
951 Bopp, L., Saltzman, E. S., Stefels, J., Johnson, J. E. and Liss, P. S.: An updated climatology
952 of surface dimethylsulfide concentrations and emission fluxes in the global ocean, *Global*
953 *Biogeochem. Cycles*, 25(1), 1–17, doi:10.1029/2010GB003850, 2011.
- 954 Lee, H., Lee, K., Lunder, C. R., Krejci, R., Aas, W., Park, J., Park, K.-T., Lee, B. Y., Yoon,
955 Y.-J. and Park, K.: Atmospheric new particle formation characteristics in the Arctic as
956 measured at Mount Zeppelin, Svalbard, from 2016 to 2018, *Atmos. Chem. Phys. Discuss.*, 1–
957 28, doi:10.5194/acp-2020-390, 2020.
- 958 Lupi, A., Busetto, M., Becagli, S., Giardi, F., Lanconelli, C., Mazzola, M., Udisti, R.,
959 Hansson, H. C., Henning, T., Petkov, B., Ström, J., Krejci, R., Tunved, P., Viola, A. Pietro
960 and Vitale, V.: Multi-seasonal ultrafine aerosol particle number concentration measurements
961 at the Gruvebadet observatory, Ny-Ålesund, Svalbard Islands, *Rend. Lincei*, 27, 59–71,
962 doi:10.1007/s12210-016-0532-8, 2016.
- 963 Mårtensson, E. M., Nilsson, E. D., de Leeuw, G., Cohen, L. H. and Hansson, H.-C.:
964 Laboratory simulations and parameterization of the primary marine aerosol production, *J.*
965 *Geophys. Res. Atmos.*, 108(D9), doi:https://doi.org/10.1029/2002JD002263, 2003.
- 966 Mikkola, J.: Slope and valley winds in the Himalayas as simulated by the Weather Research
967 and Forecasting model, , 42, 2020.



- 968 Monahan, E. C., Spiel, D. E. and Davidson, K. L.: A Model of Marine Aerosol Generation
969 Via Whitecaps and Wave Disruption, in *Oceanic Whitecaps: And Their Role in Air-Sea*
970 *Exchange Processes*, edited by E. C. Monahan and G. Mac Niocaill, pp. 167–174, Springer
971 Netherlands, Dordrecht., 1986.
- 972 Moroni, B., Ritter, C., Crocchianti, S., Markowicz, K., Mazzola, M., Becagli, S., Traversi, R.,
973 Krejci, R., Tunved, P. and Cappelletti, D.: Individual Particle Characteristics, Optical
974 Properties and Evolution of an Extreme Long-Range Transported Biomass Burning Event in
975 the European Arctic (Ny-Ålesund, Svalbard Islands), *J. Geophys. Res. Atmos.*, 125(5), 1–17,
976 doi:10.1029/2019JD031535, 2020.
- 977 Nightingale, P. D., Liss, P. S. and Schlosser, P.: Measurements of air-sea gas transfer during
978 an open ocean algal bloom, *Geophys. Res. Lett.*, 27(14), 2117–2120,
979 doi:10.1029/2000GL011541, 2000.
- 980 Noble, S. and Hudson, J. G.: Cloud supersaturations and Hoppel minima, *AIP Conf. Proc.*,
981 1527(September), 706–709, doi:10.1063/1.4803368, 2013.
- 982 Olenius, T., Kupiainen-Määttä, O., Ortega, I. K., Kurtén, T. and Vehkamäki, H.: Free energy
983 barrier in the growth of sulfuric acid-ammonia and sulfuric acid-dimethylamine clusters, *J.*
984 *Chem. Phys.*, 139(8), doi:10.1063/1.4819024, 2013.
- 985 Oshima, N., Yukimoto, S., Deushi, M., Koshiro, T., Kawai, H., Tanaka, T. Y. and Yoshida,
986 K.: Global and Arctic effective radiative forcing of anthropogenic gases and aerosols in MRI-
987 ESM2.0, *Prog. Earth Planet. Sci.*, 7(1), doi:10.1186/s40645-020-00348-w, 2020.
- 988 Öström, E., Putian, Z., Schurgers, G., Mishurov, M., Kivekäs, N., Lihavainen, H., Ehn, M.,
989 Rissanen, M. P., Kurtén, T., Boy, M., Swietlicki, E. and Roldin, P.: Modeling the role of
990 highly oxidized multifunctional organic molecules for the growth of new particles over the
991 boreal forest region, *Atmos. Chem. Phys.*, 17(14), 8887–8901, doi:10.5194/acp-17-8887-
992 2017, 2017.
- 993 Park, K. T., Jang, S., Lee, K., Yoon, Y. J., Kim, M. S., Park, K., Cho, H. J., Kang, J. H.,
994 Udisti, R., Lee, B. Y. and Shin, K. H.: Observational evidence for the formation of DMS-
995 derived aerosols during Arctic phytoplankton blooms, *Atmos. Chem. Phys.*, 17(15), 9665–
996 9675, doi:10.5194/acp-17-9665-2017, 2017.
- 997 Paulot, F., Jacob, D. J., Johnson, M. T., Bell, T. G., Baker, A. R., Keene, W. C., Lima, I. D.,
998 Doney, S. C. and Stock, C. A.: Global oceanic emission of ammonia: Constraints from
999 seawater and atmospheric observations, *Global Biogeochem. Cycles*, 29(8), 1165–1178,
1000 doi:10.1002/2015GB005106, 2015.
- 1001 Petäjä, T., Duplissy, E., Tabakova, K., Schmale, J., Altstädter, B. and Ancellet, G.: Overview :
1002 Integrative and Comprehensive Understanding on Polar Environments (iCUPE) – concept
1003 and initial results, , 8551–8592, 2020.
- 1004 Pisso, I., Sollum, E., Grythe, H., Kristiansen, N., Cassiani, M., Eckhardt, S., Arnold, D.,
1005 Morton, D., Thompson, R., Groot Zwaaftink, C., Evangeliou, N., Sodemann, H., Haimberger,
1006 L., Henne, S., Brunner, D., Burkhardt, J., Fouilloux, A., Brioude, J., Philipp, A., Seibert, P. and



- 1007 Stohl, A.: The Lagrangian particle dispersion model FLEXPART version 10.3, *Geosci. Model*
1008 *Dev. Discuss.*, (January), 1–67, doi:10.5194/gmd-2018-333, 2019.
- 1009 Quinn, P. K., Coffman, D. J., Johnson, J. E., Upchurch, L. M. and Bates, T. S.: Small fraction
1010 of marine cloud condensation nuclei made up of sea spray aerosol, *Nat. Geosci.*, 10(9), 674–
1011 679, doi:10.1038/ngeo3003, 2017.
- 1012 Rader, F., Traversi, R., Severi, M., Becagli, S., Müller, K.-J., Nakoudi, K. and Ritter, C.:
1013 Overview of Aerosol Properties in the European Arctic in Spring 2019 Based on In Situ
1014 Measurements and Lidar Data, *Atmosphere (Basel)*, 12(2), doi:10.3390/atmos12020271,
1015 2021.
- 1016 Riddick, S. N., Dragosits, U., Blackall, T. D., Daunt, F., Wanless, S. and Sutton, M. A.: The
1017 global distribution of ammonia emissions from seabird colonies, *Atmos. Environ.*, 55, 319–
1018 327, doi:10.1016/j.atmosenv.2012.02.052, 2012.
- 1019 Roldin, P., Swietlicki, E., Schurgers, G., Arneth, A., Lehtinen, K. E. J., Boy, M. and Kulmala,
1020 M.: Development and evaluation of the aerosol dynamics and gas phase chemistry model
1021 ADCHEM, *Atmos. Chem. Phys.*, 11(12), 5867–5896, doi:10.5194/acp-11-5867-2011, 2011.
- 1022 Roldin, P., Ehn, M., Kurtén, T., Olenius, T., Rissanen, M. P., Sarnela, N., Elm, J., Rantala, P.,
1023 Hao, L., Hyttinen, N., Heikkinen, L., Worsnop, D. R., Pichelstorfer, L., Xavier, C., Clusius,
1024 P., Öström, E., Petäjä, T., Kulmala, M., Vehkamäki, H., Virtanen, A., Riipinen, I. and Boy,
1025 M.: The role of highly oxygenated organic molecules in the Boreal aerosol-cloud-climate
1026 system, *Nat. Commun.*, 10(2019), 4370, doi:10.1038/s41467-019-12338-8, 2019.
- 1027 Rosati, B., Christiansen, S., Wollesen de Jonge, R., Roldin, P., Jensen, M. M., Wang, K.,
1028 Moosakutty, S. P., Thomsen, D., Salomonsen, C., Hyttinen, N., Elm, J., Feilberg, A., Glasius,
1029 M. and Bilde, M.: New Particle Formation and Growth from Dimethyl Sulfide Oxidation by
1030 Hydroxyl Radicals, *ACS Earth Sp. Chem.*, acsearthspacechem.0c00333,
1031 doi:10.1021/acsearthspacechem.0c00333, 2021.
- 1032 Rosenfeld, D., Andreae, M. O., Asmi, A., Chin, M., de Leeuw, G., Donovan, D. P., Kahn, R.,
1033 Kinne, S., Kivekäs, N., Kulmala, M., Lau, W., Schmidt, K. S., Suni, T., Wagner, T., Wild, M.
1034 and Quaas, J.: Global observations of aerosol-cloud-precipitation-climate interactions, *Rev.*
1035 *Geophys.*, 52(4), 750–808, doi:10.1002/2013RG000441, 2014.
- 1036 Salter, M. E., Zieger, P., Acosta Navarro, J. C., Grythe, H., Kirkevåg, A., Rosati, B., Riipinen,
1037 I. and Nilsson, E. D.: An empirically derived inorganic sea spray source function
1038 incorporating sea surface temperature, *Atmos. Chem. Phys.*, 15(19), 11047–11066,
1039 doi:10.5194/acp-15-11047-2015, 2015.
- 1040 Saunders, S. M., Jenkin, M. E., Derwent, R. G. and Pilling, M. J.: Protocol for the
1041 development of the Master Chemical Mechanism, MCM v3 (Part A): Tropospheric
1042 degradation of non-aromatic volatile organic compounds, *Atmos. Chem. Phys.*, 3(1), 161–
1043 180, doi:10.5194/acp-3-161-2003, 2003.
- 1044 Schemann, V. and Ebell, K.: Simulation of mixed-phase clouds with the ICON large-eddy
1045 model in the complex Arctic environment around Ny-Ålesund, *Atmos. Chem. Phys.*, 20(1),



- 1046 475–485, doi:10.5194/acp-20-475-2020, 2020.
- 1047 Scott, C. E., Rap, A., Spracklen, D. V., Forster, P. M., Carslaw, K. S., Mann, G. W., Pringle,
1048 K. J., Kivekäs, N., Kulmala, M., Lihavainen, H. and Tunved, P.: The direct and indirect
1049 radiative effects of biogenic secondary organic aerosol, *Atmos. Chem. Phys.*, 14(1), 447–470,
1050 doi:10.5194/acp-14-447-2014, 2014.
- 1051 Sofiev, M., Soares, J., Prank, M., De Leeuw, G. and Kukkonen, J.: A regional-to-global
1052 model of emission and transport of sea salt particles in the atmosphere, *J. Geophys. Res.*
1053 *Atmos.*, 116(21), doi:10.1029/2010JD014713, 2011.
- 1054 Stock, C. A., Dunne, J. P. and John, J. G.: Global-scale carbon and energy flows through the
1055 marine planktonic food web: An analysis with a coupled physical–biological model, *Prog.*
1056 *Oceanogr.*, 120, 1–28, doi:https://doi.org/10.1016/j.pocean.2013.07.001, 2014.
- 1057 Stohl, a, Sodemann, H., Eckhardt, S., Frank, a, Seibert, P. and Wotawa, G.: The Lagrangian
1058 particle dispersion model FLEXPART version 8 .2, 2005.
- 1059 Ström, J., Engvall, A. C., Delbart, F., Krejci, R. and Treffeisen, R.: On small particles in the
1060 Arctic summer boundary layer: Observations at two different heights near Ny-Ålesund,
1061 Svalbard, *Tellus, Ser. B Chem. Phys. Meteorol.*, 61 B(2), 473–482, doi:10.1111/j.1600-
1062 0889.2008.00412.x, 2009.
- 1063 Traversi, R., Becagli, S., Severi, M., Caiazzo, L., Mazzola, M., Lupi, A., Fiebig, M.,
1064 Hermansen, O., Krejci, R. and Unit, A. S.: Arctic haze in a climate changing world: the 2010-
1065 2020 trend (HAZECLIC) 4, , (0000), 104–117, 2020.
- 1066 Tunved, P., Ström, J. and Krejci, R.: Arctic aerosol life cycle: Linking aerosol size
1067 distributions observed between 2000 and 2010 with air mass transport and precipitation at
1068 Zeppelin station, Ny-Ålesund, Svalbard, *Atmos. Chem. Phys.*, 13(7), 3643–3660,
1069 doi:10.5194/acp-13-3643-2013, 2013.
- 1070 Uhlig, C., Damm, E., Peeken, I., Krumpen, T., Rabe, B., Korhonen, M. and Ludwighowski,
1071 K. U.: Sea ice and water mass influence dimethylsulfide concentrations in the central arctic
1072 ocean, *Front. Earth Sci.*, 7(July), 1–15, doi:10.3389/feart.2019.00179, 2019.
- 1073 Wainwright, C. D., Pierce, J. R., Liggio, J., Strawbridge, K. B., MacDonald, A. M. and
1074 Leaitch, R. W.: The effect of model spatial resolution on Secondary Organic Aerosol
1075 predictions: A case study at Whistler, BC, Canada, *Atmos. Chem. Phys.*, 12(22), 10911–
1076 10923, doi:10.5194/acp-12-10911-2012, 2012.
- 1077 Wentworth, G. R., Murphy, J. G., Croft, B., Martin, R. V., Pierce, J. R., Côté, J. S.,
1078 Courchesne, I., Tremblay, J. É., Gagnon, J., Thomas, J. L., Sharma, S., Toom-Sauntry, D.,
1079 Chivulescu, A., Lévassieur, M. and Abbatt, J. P. D.: Ammonia in the summertime Arctic
1080 marine boundary layer: Sources, sinks, and implications, *Atmos. Chem. Phys.*, 16(4), 1937–
1081 1953, doi:10.5194/acp-16-1937-2016, 2016.
- 1082 Wollesen de Jonge, R., Elm, J., Rosati, B., Christiansen, S., Hyttinen, N., Lüdemann, D.,
1083 Bilde, M. and Roldin, P.: Secondary aerosol formation from dimethyl sulfide – improved



- 1084 mechanistic understanding based on smog chamber experiments and modelling, *Atmos.*
1085 *Chem. Phys.*, 1–33, doi:10.5194/acp-2020-1324, 2021.
- 1086 Xavier, C., Rusanen, A., Zhou, P., Dean, C., Pichelstorfer, L., Roldin, P. and Boy, M.:
1087 Aerosol Mass yields of selected Biogenic Volatile Organic Compounds – a theoretical study
1088 with near explicit gas-phase chemistry, *Atmos. Chem. Phys. Discuss.*, 1–26, doi:10.5194/acp-
1089 2019-424, 2019.
- 1090 Zheng, G., Wang, Y., Aiken, A. C., Gallo, F., Jensen, M. P., Kollias, P., Kuang, C., Luke, E.,
1091 Springston, S., Uin, J., Wood, R. and Wang, J.: Marine boundary layer aerosol in the eastern
1092 North Atlantic: Seasonal variations and key controlling processes, *Atmos. Chem. Phys.*,
1093 18(23), 17615–17635, doi:10.5194/acp-18-17615-2018, 2018.
- 1094 Ziska, F., Quack, B., Abrahamsson, K., Archer, S. D., Atlas, E., Bell, T., Butler, J. H.,
1095 Carpenter, L. J., Jones, C. E., Harris, N. R. P., Hepach, H., Heumann, K. G., Hughes, C.,
1096 Kuss, J., Krüger, K., Liss, P., Moore, R. M., Orlikowska, A., Raimund, S., Reeves, C. E.,
1097 Reifenhäuser, W., Robinson, A. D., Schall, C., Tanhua, T., Tegtmeier, S., Turner, S., Wang,
1098 L., Wallace, D., Williams, J., Yamamoto, H., Yvon-Lewis, S. and Yokouchi, Y.: Global sea-
1099 to-air flux climatology for bromoform, dibromomethane and methyl iodide, *Atmos. Chem.*
1100 *Phys.*, 13(17), 8915–8934, doi:10.5194/acp-13-8915-2013, 2013.